3-D DIRECT NUMERICAL SIMULATION OF GAS–LIQUID AND GAS–LIQUID–SOLID FLOW SYSTEMS USING THE LEVEL-SET AND IMMERSED-BOUNDARY METHODS

Yang Ge and Liang-Shih Fan*

Department of Chemical and Biomolecular Engineering, The Ohio State University, Columbus, OH 43210, USA

Abstract

The recent advances in level-set and Immersed Boundary methods (IBM) as applied to the simulation of complex multiphase flow systems are described. Two systems are considered. For system 1, a computational scheme is conceived to describe the three-dimensional (3-D) bubble

*Corresponding author. Tel.: +1-614-688-3262(o). E-mail: fan@chbmeng.ohio-state.edu

Advances in Chemical Engineering, vol. 31
ISSN 0065-2377
DOI 10.1016/S0065-2377(06)31001-0

Copyright © 2006 by Elsevier Inc.
All rights reserved

dynamics in gas–liquid bubble columns and gas–liquid–solid fluidized beds. This scheme is utilized to simulate the motion of the gas, liquid, and solid phases, respectively, based on the level-set interface tracking method, the locally averaged time-dependent Navier–Stokes equations coupled with the Smagorinsky subgrid scale stress model, and the Lagrangian particle motion equations. For system 2, the hydrodynamics and heat-transfer phenomena of a liquid droplet in motion and during the impact process with a hot flat surface, as well as with a particle, are illustrated. The 3-D level-set method is used to portray the droplet surface deformation whilst in motion and during the impact process. The IBM is employed so that the particle–fluid boundary conditions are satisfied. The governing equations for the droplet and the surrounding gas phase are solved utilizing the finite volume method with the Arbitrary Lagrangian Eulerian (ALE) technique. To account for the multiscale effect due to lubrication-resistance induced by the vapor layer between the droplet and solid surface or solid particle formed by the film-boiling evaporation, a vapor-flow model is developed to calculate the pressure and velocity distributions along the vapor layer. The temperature fields in all phases and the local evaporation rate on the droplet surface are illustrated using a full-field heat-transfer model.

I. Introduction

Gas–liquid–solid (three-phase) flow systems involve a variety of operating modes of gas, liquid, and solid phases, including those with solid particles and/or liquid droplets in suspended states. Commercial or large-scale operations using three-phase flow systems are prevalent in physical, chemical, petrochemical, electrochemical, and biological processes (Fan, 1989). In the gas–liquid–solid fluidization systems with liquid as the continuous phase, the systems are characterized by the presence of gas bubbles, which induce significant liquid mixing and mass transfer. The flow structure in the systems is complex due to intricate coalescence and breakup phenomena of bubbles. The fundamental dynamics of solids suspensions in the systems is closely associated with the particle–particle collision and particle–bubble interactive behavior. For three-phase flows that occur in the feed nozzle area of a fluid catalytic cracking (FCC) riser in gas oil cracking, on the other hand, the gas phase is continuous where oil is injected from the nozzle with the mist droplets formed from the spray in contact with high-temperature catalyst particles (Fan *et al.*, 2001). The droplets may splash, rebound, or remain on the catalyst particle surface after the impact, and the oil is evaporated and cracked into lighter hydrocarbons. Such contact phenomena are also prevalent in the condensed mode operation of the Unipol process for

polypropylene or polyethylene production, where droplet–particle collisions in the feed nozzle are also accompanied by intense liquid evaporation. In this study, both systems involving three-phase fluidization and evaporative droplet and particle collisions are simulated using CFD based on the 3-D level-set and immersed boundary method (IBM).

CFD is a viable means for describing the fluid dynamic and transport behavior of gas–liquid–solid flow systems. There are three basic approaches commonly employed in the CFD for study of multiphase flows (Feng and Michaelides, 2005): the Eulerian–Eulerian (E-E) method, the Eulerian–Lagrangian (E-L) method, and direct numerical simulation (DNS) method. In the E-E method (Anderson and Jackson, 1967; Joseph and Lundgren, 1990; Sokolichin and Eigenberger, 1994, 1999; Zhang and Prosperetti, 1994, 2003; Mudde and Simonin, 1999), both the continuous phase and the dispersed phase, such as particles, bubbles, and droplets, are treated as interpenetrating continuous media, occupying the same space as does the continuous phase with different velocities and volume fractions for each phase. In this method, the closure relationships such as the stress and viscosity of the particle phase need to be formulated. In the E-L method, or discrete particle method (e.g., Tsuji *et al.*, 1993; Lapin and Lübbert, 1994; Hoomans *et al.*, 1996; Delnoij *et al.*, 1997), the continuous fluid phase is formulated in the Eulerian mode, while the position and the velocity of the dispersed phase, particles, or bubbles, is traced in the Lagrangian mode by solving Lagrangian motion equations. The grid size used in the computation for the continuous-phase equations is typically much larger than the object size of the dispersed phase, and the object in the dispersed phase is treated as a point source in the computational cell. With this method, the coupling of the continuous phase and the dispersion phase can be made using the Particle-Source-In-Cell method (Crowe *et al.*, 1977). The closure relationship for the interaction forces between phases requires to be provided in the E-L method.

In the DNS (Unverdi and Tryggvason, 1992a,b; Feng *et al.*, 1994a,b; Sethian and Smereka, 2003), the grid size is commonly much smaller than the object size of the dispersed phase, and the moving interface can be represented by implicit or explicit schemes in the computational domain. The velocity fields of the fluid phase are obtained by solving the Navier–Stokes equation considering the interfacial forces, such as surface tension force or solid–fluid interaction force. The motion of the object of the dispersed phase is represented in terms of a time-dependent initial-value problem. With the rapid advances in the speed and memory capacity of the computer, the DNS approach has became important in characterizing details of the complex multiphase flow field.

This paper is intended to describe recent progress on the development of the level-set method and IBM in the context of the advanced front-capturing and front-tracking methods. The paper is also intended to discuss the application of them for the 3-D DNS of two complex three-phase flow systems as described earlier.

II. Front-Capturing and Front-Tracking Methods

In the DNS of multiphase flow problems, there are various methods available for predicting interface position and movement, such as the moving-grid method, the grid-free method (Scardovelli and Zeleski, 1999) and the fixed-grid front-tracking/front-capturing method. In the moving-grid method, which is also known as the discontinuous-interface method, the interface is a boundary between two subdomains of the grid (Dandy and Leal, 1989). The grid may be structured or unstructured and even near-orthogonal, moving with the interface (Hirt *et al*., 1974). It treats the system as two distinct flows separated by a surface. When the interface moves or undergoes deformation, new, geometrically adapted grids need to be generated or remeshed (McHyman, 1984). The remeshing can be a very complicated, time-consuming process, especially when it involves a significant topology change, and/or a 3-D flow. Methods in which grids are not required include the marker particle method (Harlow and Welch, 1965) and the smoothed particle hydrodynamics method (Monaghan, 1994).

The fixed-grid method, which is also known as the continuous-interface method, employs structured or unstructured grids with the interface cutting across the fixed grids. It treats the system as a single flow with the density and viscosity varying smoothly across a finite-thickness of the interface. The numerical techniques used to solve the moving interface problem with fixed, regular grids can be categorized by two basic approaches: the front-tracking method (e.g., Harlow and Welch, 1965; Peskin, 1977; Unverdi and Tryggvason 1992a, b; Fukai *et al*., 1995) and the front-capturing method (e.g., Osher and Sethian, 1988; Sussman *et al*., 1994; Kothe and Rider, 1995; Bussmann *et al*., 1999). For a 3-D multiphase flow problem, the fixed-grid method is the most frequently used due to its efficiency and relative ease in programming.

The front-tracking method explicitly tracks the location of the interface by the advection of the Lagrangian markers on a fixed, regular grid. The marker-and-cell (MAC) method developed by Harlow and Welch (1965) was the first front-tracking technique applied in DNS, e.g., it was used by Harlow and Shannon (1967) to simulate the droplet impact on a flat surface without considering the viscosity and the surface-tension forces in the momentum-conservation equation. Fujimoto and Hatta (1996) simulated the impingement process of a water droplet on a high-temperature surface by using a single-phase 2-D MAC type solution method. The no-slip and free-slip boundary conditions are iteratively adopted on the liquid–solid interface for the spreading and recoiling process, respectively. Fukai *et al*. (1995) developed the adaptive-grid, finite-element method to track the droplet free surface in collision with a surface while considering the wettability on the contact line. The front-tracking method developed by Unverdi and Tryggvason (1992a, b) and Tryggvason *et al*. (2001) leads to many applications in the simulation of droplet or bubble flow. In this method, the location of the interface is expressed by discrete surface-marker

particles. High-order interpolation polynomials are employed to ensure a high degree of accuracy in the representation of the interface. An unstructured surface grid connecting the surface-marker particles is introduced within a volumetric grid to track the bubble front within the computational domain. Thus, discretization of the field equations is carried out on two sets of embedded meshes: (a) the Eulerian fluid grid, which is 3-D, cubical, staggered structured, and nonadaptive; and (b) the Largrangian front grid, which is 2-D, triangular, unstructured, and adaptive (Unverdi and Tryggvason 1992a, b). The infinitely thin boundary can be approximated by a smooth distribution function of a finite thickness of about three to four grid spacing. The variable density Navier–Stokes equations can then be solved by conventional Eulerian techniques (Unverdi and Tryggvason 1992a, b). This method can be numerically stiff as the density ratio of the two fluids increases, and may pose difficulties when the appearance, the connection, the detachment, and the disappearance of the gas–liquid interface are encountered. Such interface behavior occurs in the coalescence, breakup, or formation of bubbles and droplets in an unsteady flow. The front-tracking method is therefore computationally intensive. Agresar *et al.* (1998) extended the front-tracking method with adaptive refined grids near the interface to simulate the deformable circulation cell. Sato and Richardson (1994) developed a finite-element method to simulate the moving free surface of a polymeric liquid. The IBM proposed by Peskin (1977) in studying the blood flow through heart valves and the cardiac mechanics also belongs to the class of front-tracking techniques. In the IBM method, the simulation of the fluid flow with complex geometry was carried out using a Cartesian grid, and a novel procedure was formulated to impose the boundary condition at the interface. Some variants and modifications of this method were proposed in simulating various multiphase flow problems (Mittal and Iaccarino, 2005). An introduction to the IBM method is given in Section II.B.

The front-capturing method, on the other hand, is the Eulerian treatment of the interface, in which the moving interface is implicitly represented by a scalar-indicator function defined on a fixed, regular mesh point. The movement of the interface is captured by solving the advection equation of the scalar-indicator function. At every time step, the interface is generated by piecewise segments (2-D) or patches (3-D) reconstructed by this scalar function. In this method, the interfacial force, such as the surface-tension force, is incorporated into the flow-momentum equation as a source term using the continuum surface force (CSF) method (Brackbill *et al.*, 1992). This technique includes the volume of fluid (VOF) method (Hirt and Nichols, 1981; Kothe and Rider, 1995), the marker density function (MDF) (Kanai and Mtyata, 1998), and the level-set method (Osher and Sethian, 1988; Sussman *et al.*, 1994).

In the VOF method, an indicator function is defined as: 0 for a cell with pure gas, 1 for a cell with pure liquid, and 0 to 1 for a cell with a mixture of gas and liquid. An interface exists in those cells that give a VOF value of neither 0 nor 1. Since the indicator function is not explicitly associated with a particular front

grid, an algorithm is needed to reconstruct the interface. This is not an easy task, especially for a complex dynamic interface requiring 3-D calculation. Pasandideh-Ford *et al.* (1998) used a modified SOLA-VOF method to solve the momentum and heat-transfer equations for droplet deposition on a steel surface. Bussmann *et al.* (1999, 2000) developed a 3-D model to simulate the droplet collision onto an incline surface and its splash on the surface, utilizing a volume-tracking methodology. Mehdi-Nejad *et al.* (2003) also used the VOF method to simulate the bubble-entrapment behavior in a droplet when it impacts a solid surface. Karl *et al.* (1996) simulated small droplet (100–200 μm) impact onto the wall in the Leidenfrost regime using a VOF method. A free-slip boundary condition and a 180° contact angle were applied on the solid surface. Harvie and Fletcher (2001a,b) developed an axisymmetric, 2-D VOF algorithm to simulate the volatile liquid droplet impacting on a hot solid surface. The vapor flow between the droplet and solid surface was solved by a 1-D, creeping flow model, which neglects the inertial force of the flow. This model, despite being accurate at a lower *We*, failed to reproduce the droplet dynamics at a higher Weber number. Other front-capturing methods include the constrained interpolation profile (CIP) method (Yabe, 1997), and the phase-field method (Jamet *et al.*, 2001).

In the level-set method, the moving interface is implicitly represented by a smooth level-set function (Sethian and Smereka, 2003). The level-set method has proved capable of handling problems in which the interface moving speed is sensitive to the front curvature and normal direction. A significant advantage of the level-set method is that it is effective in 3-D simulation of the conditions with large topological changes, such as bubble breaking and merging, droplet–surface collisions with evaporation. In this study, the level-set technique (Sussman *et al.*, 1994) is employed to describe the motion of 3-D gas–liquid interfaces. In the following section a description of this technique is given.

A. Level-Set Method

The level-set method, which was first derived by Osher and Sethian (1988), is a versatile method for capturing the motion of a free surface in 2-D or 3-D on a fixed Eulerian grid. While similar to the VOF method, the level-set method also uses an indicator function to track the gas–liquid interface on the Eulerian grid. Instead of using the marker particles or points to describe the interface, a smooth level-set function is defined in the flow field (Sussman *et al.*, 1994). Consider a nonbody conformal Cartesian grid which is used to simulate the flow with a deformable interface Γ, as shown in Fig. 1. The whole computational domain is separated by the interface into two regions: Ω_- and Ω_+. The value of the level-set function is negative in the Ω_- region and positive in the Ω_+ region, while the interface Γ is simply described as the zero level set of

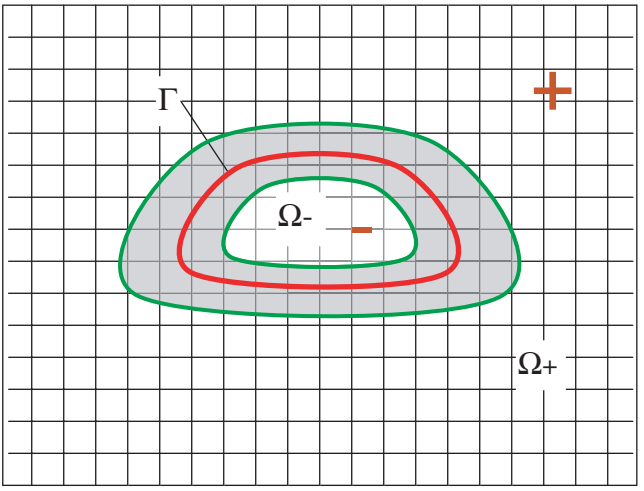

FIG. 1. The level sets of distance function for a smooth interface over a Cartesian grid.

the level-set function ϕ, i.e.,

$$\Gamma = \{x | \phi(x,t) = 0\} \tag{1}$$

where x represents the position vector and t the time. Taking $\phi < 0$ as being inside the interface Γ (in Ω_-) and $\phi > 0$ as being outside the interface Γ (in Ω_+), the level-set function has the form:

$$\phi(x,t) \begin{cases} < 0, & x \in \Omega_- \\ = 0, & x \in \Gamma \\ > 0, & x \in \Omega_+ \end{cases} \tag{2}$$

The evolution of ϕ in a flow field is given by the so-called weak-form equation:

$$\frac{\partial \phi}{\partial t} + V \cdot \nabla \phi = 0 \tag{3}$$

where V is the velocity of fluid, and is given by

$$V = \begin{cases} V_-, & x \in \Omega_- \\ V_- = V_+, & x \in \Gamma \\ V_+, & x \in \Omega_+ \end{cases} \tag{4}$$

For gas–liquid bubble flow, V_- and V_+ are the gas and liquid velocities, respectively, and the zero-level set of ϕ marks the bubble interface, which moves with time. For gas-droplets flows, on the other hand, V_- and V_+ represent the

velocity of the liquid and gas phases, respectively, and the zero-level set of ϕ defines the droplet surface (Ge and Fan, 2005).

To compute the motion of two immiscible and incompressible fluids such as a gas–liquid bubble column and gas-droplets flow, the fluid-velocity distributions outside and inside the interface can be obtained by solving the incompressible Navier–Stokes equation using level-set methods as given by Sussman *et al.* (1994):

$$\frac{\partial \rho}{\partial t} + \nabla \cdot (\rho \boldsymbol{V}) = 0 \tag{5}$$

$$\frac{\partial \rho \boldsymbol{V}}{\partial t} + \nabla \cdot (\rho \boldsymbol{V}\boldsymbol{V}) = -\nabla p + \nabla \cdot \boldsymbol{\tau} + \rho \boldsymbol{g} + \boldsymbol{F}_{\sigma} \tag{6}$$

where F_σ is the surface tension force which is calculated by (Brackbill *et al.*, 1992):

$$\boldsymbol{F}_{\sigma} = \sigma \kappa(\phi) \delta(\phi) \nabla \phi \tag{7}$$

$\kappa(\phi)$ is the curvature which can be estimated as $\nabla \cdot (\nabla\phi/|\nabla\phi|)$. A smooth δ function is defined as (Sussman *et al.*, 1998; Sussman and Fatemi, 1999):

$$\delta_{\beta}(\phi) \equiv \frac{\mathrm{d}H_{\beta}(\phi)}{\mathrm{d}\phi} = \begin{cases} \frac{1}{2}(1 + \cos(\pi\phi/\beta))/\beta, & |\phi| < \beta \\ 0, & \text{otherwise} \end{cases} \tag{8}$$

where $H_\beta(\phi)$ follows the Heaviside formulation (Sussman *et al.*, 1998; Sussman and Fatemi, 1999) given by

$$H_{\beta}(\phi) = \begin{cases} 1 & \phi > \beta \\ 0 & \phi < -\beta \\ \frac{1}{2}(1 + \frac{\phi}{\beta} + \frac{1}{\pi}\sin(\pi\phi/\beta)) & \text{otherwise} \end{cases} \tag{9}$$

The surface-tension force F_σ in Eq. (7) is smoothed and distributed into the thickness of the interface. In order to circumvent numerical instability, the fluid properties such as density and viscosity in the interface region are determined with a continuous transition:

$$\rho(\phi) = \rho_{-} + (\rho_{-} - \rho_{+}) H_{\beta}(\phi) \tag{10}$$

$$\mu(\phi) = \mu_{-} + (\mu_{-} - \mu_{+}) H_{\beta}(\phi) \tag{11}$$

Since the values for $\rho(\phi)$, $\mu(\phi)$, and the surface-tension force could be distorted if the variation of $\nabla\phi$ along the interface is very large, the thickness of the interface needs to be maintained uniformly, i.e. $|\nabla\phi| = 1$ (Sussman *et al.*, 1998). In the algorithm developed, the general level set function $\phi(x,t)$ is replaced by a

distance function $d(x,t)$, whose value represents the signed normal distance from x to the interface. $d(x,t)$ would satisfy $|\nabla d| = 1$ and $d = 0$ for $x \in \Gamma$ (Sussman *et al.*, 1998).

Even if the initial value of the level-set function $\phi(x,0)$ is set to be the distance function, the level set function ϕ may not remain as a distance function at $t > 0$ when the advection equation, Eq. (3), is solved for ϕ. Thus, a redistance scheme is needed to enforce the condition of $|\nabla\phi| = 1$. An iterative procedure was designed (Sussman *et al.*, 1998) to reinitialize the level-set function at each time step so that the level-set function remains as a distance function while maintaining the zero level set of the level-set function. This is achieved by solving for the steady-state solution of the equation (Sussman *et al.*, 1994, 1998; Sussman and Fatemi, 1999):

$$\frac{\partial d}{\partial \tau} = \text{sin}(\phi)(1 - |\nabla\phi|) \tag{12}$$

$$d(x,0) = \phi(x) \tag{13}$$

until

$$|\nabla d| = 1 + O(\Delta^2) \tag{14}$$

where the sin function is defined as

$$\text{sin}(\phi) = \begin{cases} -1, & \phi < 0 \\ 0, & \phi = 0 \\ 1, & \phi > 0 \end{cases} \tag{15}$$

In Eq. (12), τ is an artificial time that has the unit of distance. The solutions for Eq. (12) are signed distances and only those within a thickness of 3–5 grid sizes from the interface are of interest (Sussman *et al.*, 1994, 1998; Sussman and Fatemi, 1999). Equation (12) needs to be integrated for 3–5 time steps using a time step $\Delta\tau = 0.5\Delta$.

B. Immersed Boundary Method

The IBM was originally proposed by Peskin (1977) to model the blood flow through heart valves. Since then, this method has been extensively modified and extended to simulate various fluid flows in a complex geometrical configuration using a fixed Cartesian mesh (Unverdi and Tryggvason, 1992a,b; Udaykumar, *et al.*, 1997; Ye *et al.*, 1999; Fadlun *et al.*, 2000; Lai and Peskin, 2000; Kim *et al.*, 2001). In the IBM, the presence of the solid object in a fluid field is represented by a virtual-body force field, which is applied on the computational grid in the vicinity of the solid–flow interface through a Dirac delta function (Lai and

Peskin, 2000). Various schemes have been proposed to calculate the virtual force density in the literature. Goldstein *et al.* (1993) developed a virtual boundary formulation to simulate the startup flow over a cylinder. In their formation, the virtual force field is calculated in a feedback manner in order to satisfy the boundary condition at the solid surface. Mohd-Yusof (1997) developed an alternative direct forcing scheme to evaluate the virtual force based on the N-S equation at discrete times. Fadlum *et al.* (2000) extended the direct forcing scheme of Mohd-Yusof (1997) to a 3-D finite-difference method. Instead of evaluating and applying the virtual force, the velocity at the first grid point outside the solid boundary is estimated through a linear interpolation of the moving velocity of the boundary and the velocity at the second external grid point. Conceptually, this velocity interpolation scheme is equivalent to applying the momentum force inside the flow field (Kim *et al.*, 2001). This scheme is more efficient in 3-D because it has no adjustable constant and has no extra restriction on the scale of the time step, which is required in the feedback-forcing scheme. Kim *et al.* (2001) simulated the flow over complex geometry in a finite-volume approach with staggered meshes. The momentum force and mass source were applied on the immersed boundary to satisfy the no-slip boundary condition and the flow continuity.

The basic idea of the IBM is that the presence of the solid boundary (fixed or moving) in a fluid can be represented by a virtual body force field $\vec{F}_p$ applied on the computational grid at the vicinity of solid–flow interface. Thus, the Navier–Stokes equation for this flow system in the Eulerian frame can be given by

$$\frac{\partial \rho \boldsymbol{V}}{\partial t} + \nabla \cdot (\rho \boldsymbol{V}\boldsymbol{V}) = -\nabla p + \nabla \cdot \boldsymbol{\tau} + \rho \boldsymbol{g} + \vec{F}_p \tag{16}$$

It is noted that the virtual body force $\vec{F}_p$ depends not only on the unsteady fluid velocity, but also on the velocity and location of the particle surface, which is also a function of time. There are several ways to specify this boundary force, such as the feedback forcing scheme (Goldstein *et al.*, 1993) and direct forcing scheme (Fadlun *et al.*, 2000). In 3-D simulation, the direct forcing scheme can give higher stability and efficiency of calculation. In this scheme, the discretized momentum equation for the computational volume on the boundary is given as

$$V^{t+1} = V^t + \Delta t(RHS^t + F_p^t) \tag{17}$$

where RHS refers to all the terms in the right-hand side of Eq. (16) except the virtual body force $\vec{F}_p$. The virtual body force F^t_p is used to maintain the fluid velocity to be equal to the particle velocity at the particle surface (i.e., no-slip boundary condition), which is

$$V^{t+1} = V_p(t) \tag{18}$$

where V_p is the particle velocity. Thus, the discrete virtual force can be defined as

$$F_p^t = (V_p - V^t)/\Delta t - RHS^t \tag{19}$$

Since the computational grids are generally not coincident with the location of the particle surface, a velocity interpolation procedure needs to be carried out in order to calculate the boundary force and apply this force to the control volumes close to the immersed particle surface (Fadlun *et al.*, 2000).

Other than the virtual momentum force $\vec{F}_p$, a virtual mass source/sink should also be applied to the particle surface to satisfy the continuity for the control volume containing the particle surface or the particle (Kim *et al.*, 2001). The mass source can be calculated by

$$q^t = \frac{1}{\Delta V}\sum_i \alpha_i \vec{V}_i^t \cdot \vec{n}_i \Delta s_i \tag{20}$$

where ΔV is the volume of the computation cell (control volume) and Δs_i the surface area of surface i of this cell. For a 3-D case, $i = 1, 2, \ldots, 6$. $\vec{n}_i$ is the normal vector of each face of the cell. $\vec{V}_i^t$ the fluid velocity at each face of the cell. α_i the flag to indicate whether the virtual body force is applied to face i of the cell or not. $\alpha_i = 1$ when the force is applied, otherwise it is zero. Therefore, the continuity equation of the incompressible fluid can be written as (Kim *et al.*, 2001):

$$\nabla \cdot \vec{V} = q \tag{21}$$

III. System 1: Flow Dynamics of Gas–Liquid–Solid Fluidized Beds

The flows in a gas–liquid–solid fluidized bed or a gas–liquid bubble column are represented by two regimes, the homogeneous and the heterogeneous. In the homogenous regime, the coalescence of bubbles does not occur and there is little variation of bubble sizes. However, this is not the case in the heterogeneous regime. The flow structure in the heterogeneous regime is complex due to substantial coalescence and breakup of bubbles. Both the E-E and the E-L methods have proven to be more effective in modeling the homogenous regime than the heterogeneous regime of gas–liquid flow. In the simulation of the heterogeneous regime of gas–liquid flows using either the E-E or the E-L method, the challenge lies in the establishment of an accurate closure relationship for the interphase momentum exchange. The interphase momentum exchange is induced through the drag force that liquid exerts on the bubble surface, the virtual mass force due to the bubble and liquid inertial motion, and the lift force caused by the shear flows around the bubbles. In gas–liquid bubble columns and gas–liquid–solid

fluidized systems, the interstitial forces under the bubble coalescence and breakup conditions are not well established. A computational model based on the level-set methods given below provides some information on the much needed closure relationship of the interphase momentum exchange noted above.

A. Numerical Procedure for Solving the Gas–Liquid Interface

The level-set technique described in Section II.A is employed to capture the motion of 3-D gas–liquid interfaces. The numerical procedures for solving the gas–liquid interface include finding the solution for the time-dependent Eqs. (3), (5), and (6). Given $\phi_{\mathrm{n}}$and V_{n}defined at cell centers at one time instant t_n, ϕ_{n+1}, and V_{n+1} can be solved over a time increment at a new time instant $t_{n+1} = t_n + \Delta t$ following the procedures given below:

Solve Eqs. (5) and (6) to obtain the velocity distribution in the flow field V_{n+1} using the Arbitrary-Lagrangian-Eulerian (ALE) scheme (Kashiwa *et al.*, 1994).

Solve Eq. (3) to obtain ϕ_{n+1} using the second-order TVD-Runge-Kutta method presented as follows:

$$\bar{\phi}_{n+1} = \phi_n + \Delta t \phi_{tn} \tag{22}$$

$$\phi_{n+1} = \phi_n + \frac{\Delta t}{2}(\bar{\phi}_{tn+1} + \phi_{tn}) \tag{23}$$

where $\phi_{tn} = -V_n \Delta \phi_n$ and the time steps are the same as that used in calculating V_{n+1}, which is determined by restrictions due to the Courant–Friedrichs–Levy (CFL) condition, gravity, viscosity, and surface tension.

Solve Eq. (12) to perform the redistancing.

Although, in principle, Eq. (12) would not alter the location of the zero-level set of ϕ, in practice, with numerical computation it may not be true. A redistance operation is needed to maintain the volume conservation. Therefore, Eq. (12) is modified to (Sussman *et al.*, 1998):

$$\frac{\partial d}{\partial \tau} = \sin(\phi)(1 - |\nabla \phi|) + \lambda_{ij} f(\phi) \equiv L(\phi, d) + \lambda_{ij} f(\phi) \tag{24}$$

where

$$\lambda_{ij} = \frac{\int_{\Omega_{ij}} \mathrm{H}'(\phi) L(\phi, d)}{\int_{\Omega_{ij}} \mathrm{H}'(\phi) f(\phi)} \tag{25}$$

and

$$f(\phi) \equiv H'(\phi)|\nabla \phi| \tag{26}$$

B. Governing Equations for the Gas–Liquid–Solid Flow

The gas–liquid–solid flow is characterized by a wide range of physical length scales, including small to large eddies in the bubble wake, and size in the millimeter range for solid particles and in the millimeter/centimeter range for gas bubbles. The accurate description of the gas bubble surface and bubbling flow requires the use of fine grids, while the tracking of the motion of solid particles needs the grid size to be much larger than the particle sizes.

For simulation of a gas–liquid–solid fluidized bed, the locally averaged Navier–Stokes equations (Anderson and Jackson, 1967) are used to describe the liquid phase flow outside the gas bubble, and the gas phase flow inside the gas bubble. Due to the large grid size used, the liquid phase turbulence needs to be considered. In this study, a modified coefficient that illustrates the effect of the bubble-induced turbulence for a subgrid scale (SGS) stress model is employed. The level-set method and the numerical procedures described in Sections II.A and III. are used to simulate the motion and the topological variation of the gas bubble. The locally averaged governing equations of Eqs. (5) and (6) for liquid flow outside the bubble and gas flow inside the bubble are given as:

$$\frac{\partial \varepsilon\rho}{\partial t} + \nabla \cdot (\varepsilon\rho \boldsymbol{V}) = 0 \tag{27}$$

$$\frac{\partial \varepsilon\rho \boldsymbol{V}}{\partial t} + \nabla \cdot (\varepsilon\rho \boldsymbol{V}\boldsymbol{V}) = -\varepsilon\nabla p + \varepsilon\nabla \cdot \boldsymbol{\tau} - \varepsilon\nabla \cdot \boldsymbol{\tau}^{sg} + \varepsilon\rho \boldsymbol{g} + \boldsymbol{F}_D + \varepsilon \boldsymbol{F}_\sigma \tag{28}$$

ε represents the void fraction of liquid or gas and satisfies:

$$\varepsilon + \varepsilon_p = 1 \tag{29}$$

where ε_p is the void fraction of solid particles. τ^{sg} the SGS stress term. It is modeled by the Smagorinsky (1963) model written as

$$\boldsymbol{\tau}_{ij}^{\mathrm{sg}} = -v_T \left(\frac{\partial \boldsymbol{V}_i}{\partial x_j} + \frac{\partial \boldsymbol{V}_j}{\partial x_i} \right) \tag{30}$$

where v_{T} is defined as

$$v_T = (C_{\mathrm{s}} l)^2 |S| \tag{31}$$

for bulk flow, and

$$v_T = C_{\mathrm{s}} f(y) l^2 |S| \tag{32}$$

for walls with a wall function $f(y)$. C_{s} is the Smagorinsky coefficient, $l = \Delta$, and

$$|S| \equiv \sqrt{2 S_{ij} S_{ij}} \tag{33}$$

The volumetric fluid–particle interaction force F_D in Eq. (28) is calculated from the forces acting on the individual particles in a cell:

$$\boldsymbol{F}_D = -\frac{\sum \boldsymbol{f}_d^k}{\Delta\Omega_{ij}}, \tag{34}$$

where f_d is the fluid–particle interaction force for a single particle and $\Delta\Omega$ the cell volume.

C. Modeling the Motion and Collision Dynamics of Solid Particles in Gas–Liquid–Solid Fluidization

The motion of a particle in the flow field can be described in the Lagrangian coordinate with the origin placed at the center of the moving particle. There are two modes of particle motion, translation and rotation. Interparticle collisions result in both the translational and the rotational movement, while the fluid hydrodynamic forces cause particle translation. Assuming that the force acting on a particle can be determined exclusively from its interaction with the surrounding liquid and gas, the motion of a single particle without collision with another particle can be described by Newton's second law as

$$\frac{\mathrm{d}\mathbf{x}_p}{\mathrm{d}t} = \boldsymbol{V}_p \tag{35}$$

$$m_p \frac{\mathrm{d}\boldsymbol{V}_p}{\mathrm{d}t} = m_p \boldsymbol{g} + \frac{\pi}{6} d_p^3 (-\nabla p + \nabla \cdot \boldsymbol{\tau} - \nabla \cdot \boldsymbol{\tau}^{sg}) + \boldsymbol{f}_d + \boldsymbol{f}_{am} + \boldsymbol{f}_\sigma \tag{36}$$

where x_p and V_p are the particle position and particle velocity, respectively, and d_p the diameter of the particle. The five terms on the right-hand side of Eq. (36) represent, respectively, the gravity force, the fluid stress gradient force, the total drag force, the added mass force and the bubble-surface-tension-induced force. The Saffman, the Magnus, and the Basset forces are ignored.

Note that the lubrication effect due to particle collisions in liquid is significant. The liquid layer dynamics pertaining to the lubrication effect was examined by Zenit and Hunt (1999). Zhang *et al.* (1999) used a Lattice-Boltzmann (LB) simulation to account for a close-range particle collision effect and developed a correction factor for the drag force for close-range collisions, or the lubrication effect. Such a term has been incorporated in a 2-D simulation based on the VOF method (Li *et al.*, 1999). Equation (36) does not consider the lubrication effect. Clearly, this is a crude assumption. However, in the three-phase flow simulation, this study is intended to simulate only the dilute solids suspension condition ($\varepsilon_p = 0.42$–3.4%) with the bubble flow time of less than 1 s starting when bubbles are introduced to the solids suspension at a prescribed ε_p.

The particle collision effect under this simulation condition, therefore, would be small.

Note that depending on the manner in which the drag force and the buoyancy force are accounted for in the decomposition of the total fluid–particle interactive force, different forms of the particle motion equation may result (Jackson, 2000). In Eq. (36), the total fluid–particle interaction force is considered to be decomposed into two parts: a drag force ($\boldsymbol{f}_d$) and a fluid stress gradient force (see Eq. (2.29) in Jackson, 2000)). The drag force can be related to that expressed by the Wen–Yu equation, $f_{\text{Wen–Yu}}$, by

$$\boldsymbol{f}_d = \varepsilon \boldsymbol{f}_{\text{Wen–Yu}} \tag{37}$$

The Wen and Yu (1966) equation is given by

$$\boldsymbol{f}_{\text{Wen–Yu}} = \frac{1}{8}\pi d_{\text{p}}^2 C_{\text{D}} \varepsilon^2 \rho \left| \boldsymbol{V} - \boldsymbol{V}_{\text{p}} \right| (\boldsymbol{V} - \boldsymbol{V}_{\text{p}}) \tag{38}$$

where the effective drag coefficient C_{D} is calculated by

$$C_{\text{D}} = C_{\text{D0}} \varepsilon^{-4.7} \tag{39}$$

In Eq. (39), C_{D0} is a function of the particle Reynolds number, $Re_{\text{p}} = \rho \varepsilon d_{\text{p}} |\boldsymbol{V} - \boldsymbol{V}_{\text{p}}| / \mu$. For rigid spherical particles, the drag coefficient C_{D0} can be estimated by the following equations (Rowe and Henwood, 1961):

$$C_{\text{D0}} = \begin{cases} \frac{24}{Re_{\text{p}}}(1 + 0.15(Re_{\text{p}})^{0.687}), & Re_{\text{p}} < 1000 \\ 0.44, & Re_{\text{p}} \geq 1000 \end{cases} \tag{40}$$

The added mass force accounts for the resistance of the fluid mass that is moving at the same acceleration as the particle. Neglecting the effect of the particle concentration on the virtual-mass coefficient, for a spherical particle, the volume of the added mass is equal to one-half of the particle volume, so that

$$\boldsymbol{f}_{\text{am}} = \frac{1}{12}\pi d_{\text{p}}^3 \rho \left(\frac{D\boldsymbol{V}}{Dt} - \frac{D\boldsymbol{V}_{\text{p}}}{Dt} \right) \tag{41}$$

When particles approach the gas–liquid interface, the surface-tension force acts on the particles through the liquid film. The bubble-surface-tension induced force can be described by

$$f_\sigma = \frac{\pi}{6} d_{\text{p}}^3 \sigma K(\phi) \delta(\phi) \nabla \phi \tag{42}$$

When the particle inertia overcomes the surface-tension-induced force, the particle will penetrate the bubbles. Recognizing that particle penetration may not lead to bubble breakage, details of bubble instability due to particle collision are given in Chen and Fan (1989a, b).

To simulate the particle–particle collision, the hard-sphere model, which is based on the conservation law for linear momentum and angular momentum, is used. Two empirical parameters, a restitution coefficient of 0.9 and a friction coefficient of 0.3, are utilized in the simulation. In this study, collisions between spherical particles are assumed to be binary and quasi-instantaneous. The equations, which follow those of molecular dynamic simulation, are used to locate the minimum flight time of particles before any collision. Compared with the soft-sphere particle–particle collision model, the hard-sphere model accounts for the rotational particle motion in the collision dynamics calculation; thus, only the translational motion equation is required to describe the fluid induced particle motion. In addition, the hard-sphere model also permits larger time steps in the calculation; therefore, the simulation of a sequence of collisions can be more computationally effective. The details of this approach can be found in the literature (Hoomans *et al.*, 1996; Crowe *et al.*, 1998).

D. Results and Discussions

The computation performed in this study is based on the model equations developed in this study as presented in Sections II.A, III.A, III.B, and III.C These equations are incorporated into a 3-D hydrodynamic solver, CFDLIB, developed by the Los Alamos National Laboratory (Kashiwa *et al.*, 1994). In what follows, simple cases including a single air bubble rising in water, and bubble formation from a single nozzle in bubble columns are first simulated. To verify the accuracy of the model, experiments are also conducted for these cases and the experimental results are compared with the simulation results. Simulations are performed to account for the bubble-rise phenomena in liquid–solid suspensions with single nozzles. Finally, the interactive behavior between bubbles and solid particles is examined. The bubble formation and rise from multiple nozzles is simulated, and the limitation of the applicability of the models is discussed.

1. Single Air Bubble Rising in Water

The simulation for a single air bubble rising in water (density: $0.998\,\mathrm{kg/cm^3}$; viscosity: $0.01\,\mathrm{Pa\cdot s}$; surface tension: 0.0728 N/m) is performed in a $4 \times 4 \times 8\,\mathrm{cm^3}$ 3-D column. A uniform grid size of 0.05 cm is used for three dimensions which generates $80 \times 80 \times 160$ ($= 1.024 \times 10^6$) grid points in the computational domain. Initially, a spherical air bubble is positioned at rest in this domain with its center located 0.5 cm above the bottom and the liquid is quiescent. The free-slip boundary conditions are imposed on all six walls. Note that the dimension of the computational domain is selected based on numerical experiments. It is found that, under both free-slip and no-slip wall boundary conditions, when the distance of the bubble interface to the wall is more than twice as large as the

bubble diameter, there is practically little effect of the wall boundary conditions on the simulation results. Thus, with an exception of the cases involving several bubbles which migrate to the near-wall region through the zigzag motion that will be discussed in a later section, the simulation results obtained in this study are not affected by these wall boundary conditions. The time for an air bubble of 0.8 cm in diameter rising from the initial position to the outlet of the column is about 0.4 s, which corresponds to a bubble rise velocity of 18.75 cm/s. The simulation was conducted using a Cray SV1 supercomputer at the Ohio Supercomputer Center (OSC). The CPU time to compute the entire process of bubble rising is 4 h.

The simulation results for the positions and the shape changes of the 0.8 cm air bubble rising in water are shown in Fig. 2. The value for the Eotvos number ($E_0 = g\Delta\rho d_e^2/\sigma$) and the Morton number ($M = g\mu^4\Delta\rho/\rho^2\sigma^3$) are 8.5 and 2.5×10^{-7}, respectively. The time increment between two bubble images in Fig. 2 is 0.05 s. As seen in the figure, the bubble shape undergoes continuous changes from a sphere initially to an oblate ellipsoidal cap, and fluctuates between an oblate ellipsoidal cap and a spherical cap. The rectilinear motion of a bubble in water exhibited in the figure, occurs for the first several fractions of a second of a single bubble rising (with symmetric wakes) in a quiescent liquid even though the bubble Reynolds number (Re_b) is in the wake shedding regime ($Re_b > 400$). The computed results obtained in this study capture such

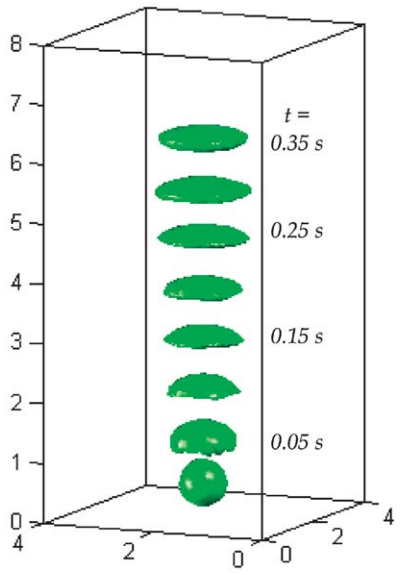

FIG. 2. Simulated positions and shape variations of a rising bubble in a water column. Initial bubble diameter 0.8 cm and time increment 0.05 s.

phenomena well. The liquid-field disturbance would eventually induce an asymmetric wake, yielding wake-shedding phenomena of the rising bubble.

The mesh-refinement studies are conducted to examine the mesh effect on the computation results. Simulations of a 0.8 cm air bubble rising in a $4 \times 4 \times 8\,\text{cm}^3$ water column (as shown in Fig. 2) are repeated at three different mesh resolutions: from a lower resolution of $40 \times 40 \times 80$ grid points with a grid size of 0.1 cm to a higher resolution of $100 \times 100 \times 200$ grid points with a grid size of 0.04 cm. The simulated variations of bubble rise velocity and bubble aspect ratio (height/width) with time are shown in Figs. 3a and b, respectively.

Fig. 3a indicates that the bubble-rise velocity measured based on the displacement of the top surface of the bubble (U_{bt}) quickly increases and approaches the terminal bubble rise velocity in 0.02 s. The small fluctuation of U_{bt} is caused by numerical instability. The bubble-rise velocity measured based on the displacement of the bottom surface of the bubble (U_{bb}) fluctuates significantly with time initially and converges to U_{bt} after 0.25 s. The overshooting of U_{bb} can reach 45–50 cm/s in Fig. 3a. The fluctuation of U_{bb} reflects the unsteady oscillation of the bubble due to the wake flow and shedding at the base of the bubble. Although the relative deviation between the simulation results of the $40 \times 40 \times 80$ mesh and $100 \times 100 \times 200$ mesh is notable, the deviation is insignificant between the results of the $80 \times 80 \times 160$ mesh and those of the $100 \times 100 \times 200$ mesh. The agreement with experiments at all resolutions is generally reasonable, although the simulated terminal bubble rise velocities ($\sim$20 cm/s) are slightly lower than the experimental results (21$\sim$25 cm/s). A lower bubble-rise velocity obtained from the simulation is expected due to the no-slip condition imposed at the gas–liquid interface, and the finite thickness for the gas–liquid interface employed in the computational scheme.

The aspect ratio shown in Fig. 3b describes the change of the bubble shape with time during the bubble rising. The simulation and the experimental results generally agree well, as shown in the figure. It can also be seen that the simulation results are only sensitive to the mesh size of $40 \times 40 \times 80$ mesh and the deviation between the results of $80 \times 80 \times 160$ mesh and $100 \times 100 \times 200$ mesh is small. Thus, Figs. 3a and b indicate that a reasonable accuracy can be reached in this bubble-rise simulation with a $80 \times 80 \times 160$ mesh (grid size of 0.05 cm).

The simulation results on bubble velocities, bubble shapes, and their fluctuation shown in Fig. 3 are consistent with the existing correlations (Fan and Tsuchiya, 1990) and experimental results obtained in this study. Bubble rise experiments were conducted in a 4 cm $\times$ 4 cm Plexiglas bubble column under the same operating conditions as those of the simulations. Air and tap water were used as the gas and liquid phases, respectively. Gas is introduced through a 6 mm nozzle. Note that water contamination would alter the bubble-rise properties in the surface tension dominated regime. In ambient conditions, this regime covers the equivalent bubble diameters from 0.8 to 4 mm (Fan and Tsuchiya, 1990). All the air–water experiments and simulations of this study are carried out under the condition where most equivalent bubble diameters exceed

4 mm.These flow conditions correspond to the bubble inertial regime, and thus, the extent of water contamination plays a negligible role in the determination of the bubble-rise properties.

The thickness of the gas–liquid interface is set as 3Δ based on the parameters used in the case of Sussman (1998), with the same density-ratio on the interface and similar Reynolds number. An interface thickness of 5Δ is also examined in the simulation and no significant improvement is observed. The accurate prediction of the bubble shape (shown in Figs. 3 and 4) can be attributed, in part, to the manner in which the surface-tension force is treated as a body force in the computation scheme. Specifically, since the surface-tension force acting on a solid particle is considered only when a solid particle crosses the gas–liquid interface and the solid particle is considered as a point, the accuracy of the calculation of this force can be expected if the surface tension is interpreted as a body force acting on each grid node near the interface.

2. *Bubble Formation from an Orifice*

The air-bubble formation from a single orifice in water is simulated. The computational domain is $2 \times 2 \times 4\,\text{cm}^3$. A uniform grid size of 0.025 cm and $80 \times 80 \times 160$ grid points are used to obtain convergent solutions for the bubble formation process. This mesh-size effect is examined by comparing the simulation results on the bubble-formation processes with experimental measurements. As shown in Fig. 4, decreasing the mesh size or increasing the mesh resolution from $40 \times 40 \times 80$ to $80 \times 80 \times 160$ improves the accuracy of the prediction results on the bubble shape. Further increase in mesh resolution does not practically change the simulation results.

Simulations are then performed for gas bubbles emerging from a single nozzle with 0.4 cm I.D. at an average nozzle velocity of 10 cm/s. The experimental measurements of inlet gas injection velocity in the nozzle using an FMA3306 gas flow meter reveals an inlet velocity fluctuation of 3–15% of the mean inlet velocity. A fluctuation of 10% is imposed on the gas velocity for the nozzle to represent the fluctuating nature of the inlet gas velocities. The initial velocity of the liquid is set as zero. An inflow condition and an outflow condition are assumed for the bottom wall and the top walls, respectively, with the free-slip boundary condition for the side walls.

Fig. 5 shows the simulated air-bubble formation and rising behavior in water. For the first three bubbles, the formation process is characterized by three distinct stages of expansion, detachment, and deformation. In comparison with the bubble formation in the air–hydrocarbon fluid (Paratherm) system, the coalescence of the first two bubbles occurs much earlier in the air–water system. Note that the physical properties of the Paratherm are $\rho_l = 870\,\text{kg/m}^3$, $\mu_l = 0.032\,\text{Pa}\cdot\text{s}$, and $\sigma = 0.029\,\text{N/m}$ at 25 °C and 0.1 MPa. This is due to the fact that, compared to that in the air–Paratherm system, the first bubble in the air–water system is much larger in size and hence higher in rise velocity leading

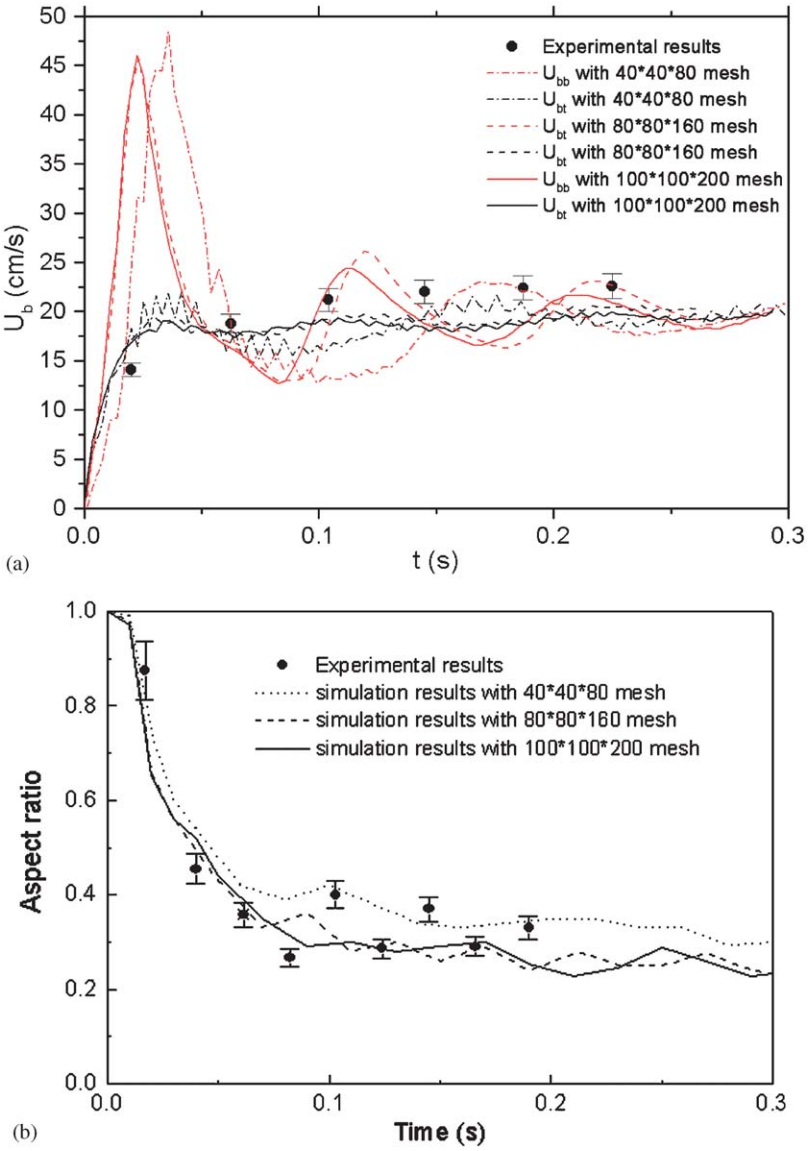

FIG. 3. (a) Comparison of the simulation results and experimental results of the bubble rise velocity. (b) Comparison of the simulation and experimental results of the bubble aspect ratio.

to a longer time for its coalescence with the second bubble. Beginning with the third bubble, the formation and rising behavior of air bubbles in water shows strongly asymmetric behavior. As is evident from Fig. 5, the bubble rises in a spiral path or a zigzag path.

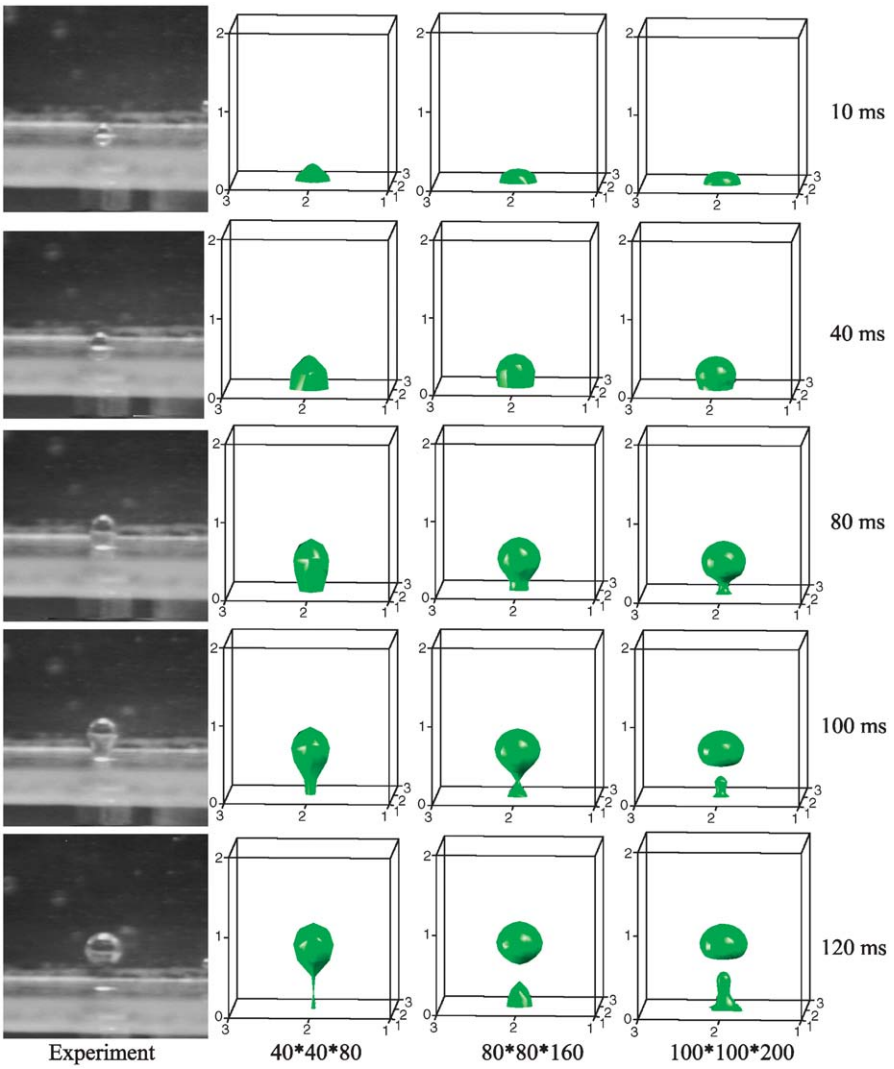

FIG. 4. Comparison of the experimental measurement and the simulation results with different resolutions of air-bubble formation in water.

In order to verify the simulation results, experiments on bubble behavior in bubble columns are carried out under conditions similar to the simulations. A 3-D rectangular bubble column with the dimension of $8 \times 8 \times 20\,\text{cm}^3$ is used for the experiments. Four nozzles with 0.4 cm I.D. and a displacement of 2.4 cm are designed in the experiments. For single-nozzle experiments, air is injected into the liquid bed through one of the orifices while the others are shut off. The outlet air velocity from the nozzle is approximated using the measured bubbling

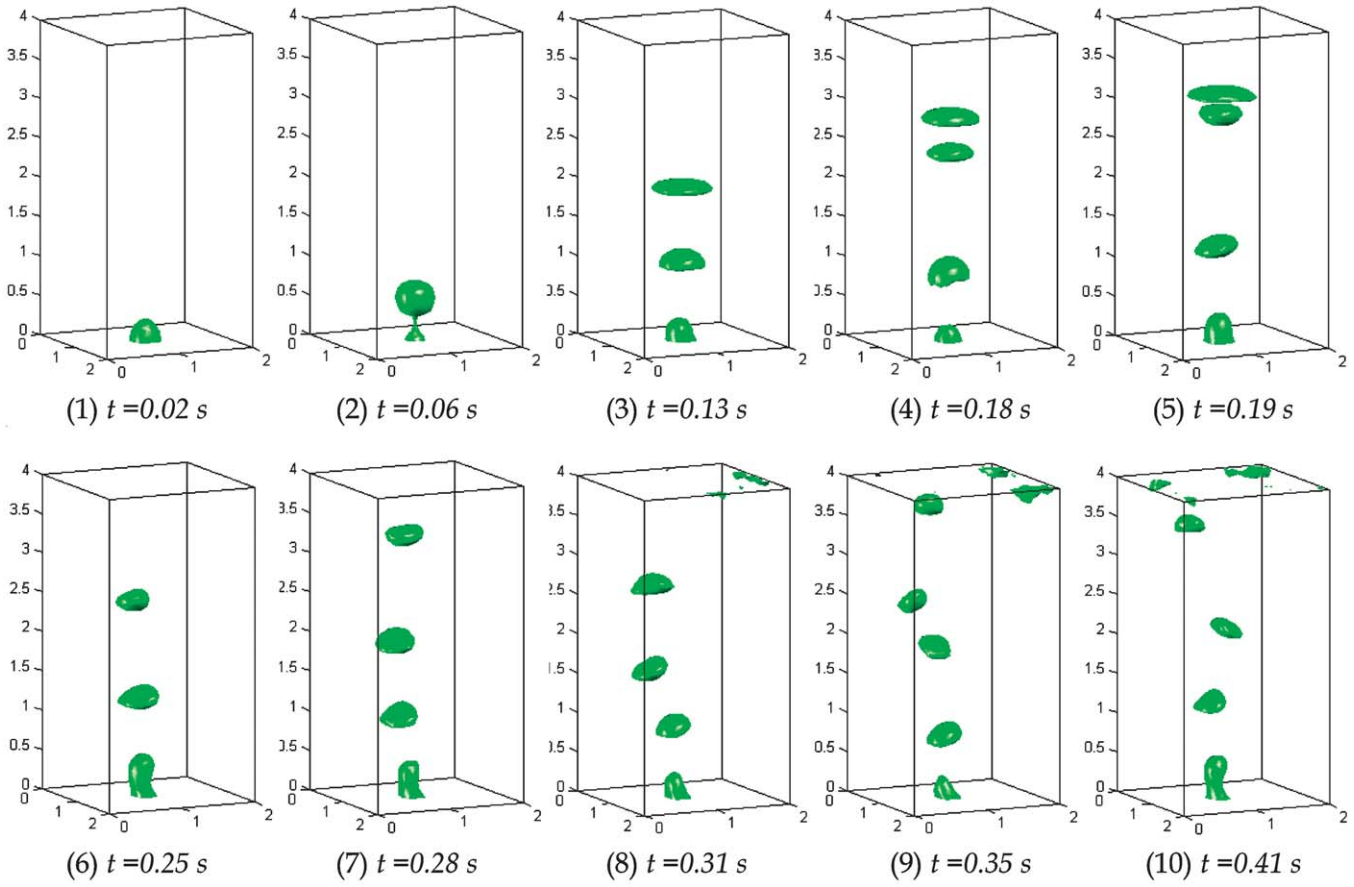

FIG. 5. Simulation results of air-bubble formation from a single nozzle in water. Nozzle size 0.4 cm I.D. and nozzle gas velocity 10 cm/s.

frequency and the initial bubble size. A high-speed video camera (240 frames/s) is used to obtain the images of bubbles emerging from the orifice in the liquid.

A common dimensionless number used to characterize the bubble formation from orifices through a gas chamber is the capacitance number defined as: $N_c = 4V_c g\rho_l/\pi D_0^2 P_s$. For the bubble-formation system with inlet gas provided by nozzle tubes connected to an air compressor, the volume of the gas chamber is negligible, and thus, the dimensionless capacitance number is close to zero. The gas-flow rate through the nozzle would be near constant. For bubble formation under the constant flow rate condition, an increasing flow rate significantly increases the frequency of bubble formation. The initial bubble size also increases with an increase in the flow rate. Experimental results are shown in Fig. 6. Three different nozzle-inlet velocities are used in the air–water experiments. It is clearly seen that at all velocities used for nozzle air injection, bubbles rise in a zigzag path and a spiral motion of the bubbles prevails in air–water experiments. The simulation results on bubble formation and rise behavior conducted in this study closely resemble the experimental results.

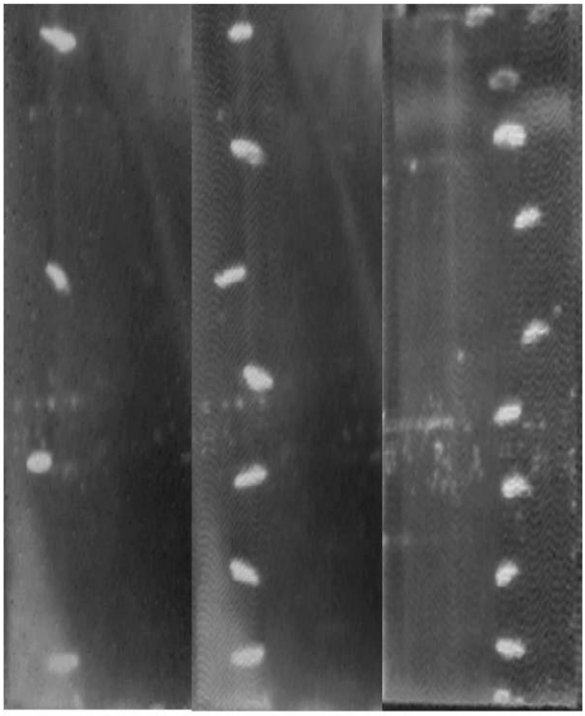

FIG. 6. Experimental results on air-bubble formation and bubble rising in water. Nozzle size 0.4 cm I.D. and nozzle gas velocity (a) ~6.0 cm/s; (b) ~10.0 cm/s; (c) ~14 cm/s.

3. *Gas–Liquid–Solid Fluidization*

As noted earlier, to simulate the bubble motion in a gas–liquid bubble column accurately, fine grid sizes, 0.025 cm for air–water and 0.05 cm for air–Paratherm system, should be used in the computation. This fine-grid computation yields essentially the results of DNS. These grid sizes are smaller than the size of the solid particle usually employed for the three-phase fluidized bed operation. For the particle size of 0.08 cm used in the present simulation of a three-phase fluidized bed, the computational grid size is required to be no less than 0.2 cm in order to track both the bubble flow and the particle motion. Note that the system simulated in this study is a dilute liquid–solid bed with a minimum of particle–particle collisions and uniform particle distribution. Although a grid size of $\Delta > 10\ D_p$ as generally used in the Lagrangian simulation of fluid–particle flows is preferable, the grid size used under the current simulation of three-phase flows is acceptable. There were no numerical stability or convergence problems encountered in the computation. For simulation of the bubble formation in a gas–liquid bubble column, a coarse grid size of 0.2 cm in a $4 \times 4 \times 8\ \text{cm}^3$ domain with $21 \times 21 \times 41$ grid points is used in this study. However, due to this large grid size used, without any turbulence model, the simulation cannot accurately track the discrete bubble-formation process. Specifically, simulation without consideration of the turbulent effects, the bubbles with distorted wake structure are seen to be connected like a jet above a nozzle. An SGS stress model is thus employed and incorporated into the code for subsequent simulation. The simulation of the gas–liquid bubble column system indicates that experimental results on a bubble formation in an air–Paratherm medium can be well described when C_s values are in a range of 1.0 to 1.2 with a grid size of 0.2 cm.Note that the values for the Smagorinsky coefficient for single phase flow are 0.1–0.2. The results are shown in Fig. 7(a).

Subsequently, simulations are performed for the air–Paratherm–solid fluidized bed system with solid particles of 0.08 cm in diameter and $0.896\ \text{g/cm}^3$ in density. The solid particle density is very close to the liquid density ($0.868\ \text{g/cm}^3$). The boundary condition for the gas phase is inflow and outflow for the bottom and the top walls, respectively. Particles are initially distributed in the liquid medium in which no flows for the liquid and particles are allowed through the bottom and top walls. Free slip boundary conditions are imposed on the four side walls. Specific simulation conditions for the particles are given as follows: Case (b) 2,000 particles randomly placed in a $4 \times 4 \times 8\ \text{cm}^3$ column; Case (c) 8,000 particles randomly placed in a $4 \times 4 \times 8\ \text{cm}^3$ column; and Case (d) 8,000 particles randomly placed in the lower half of the $4 \times 4 \times 8\ \text{cm}^3$ column. The solids volume fractions are 0.42, 1.68, and 3.35%, respectively for Cases (b), (c), and (d).

The bubble-formation process at different solids concentrations is shown in Figs. 7(b)–(d) and is compared with that without particles as shown in Fig. 7(a). For the first 0.3 s, little change is observed in the bubble-formation process

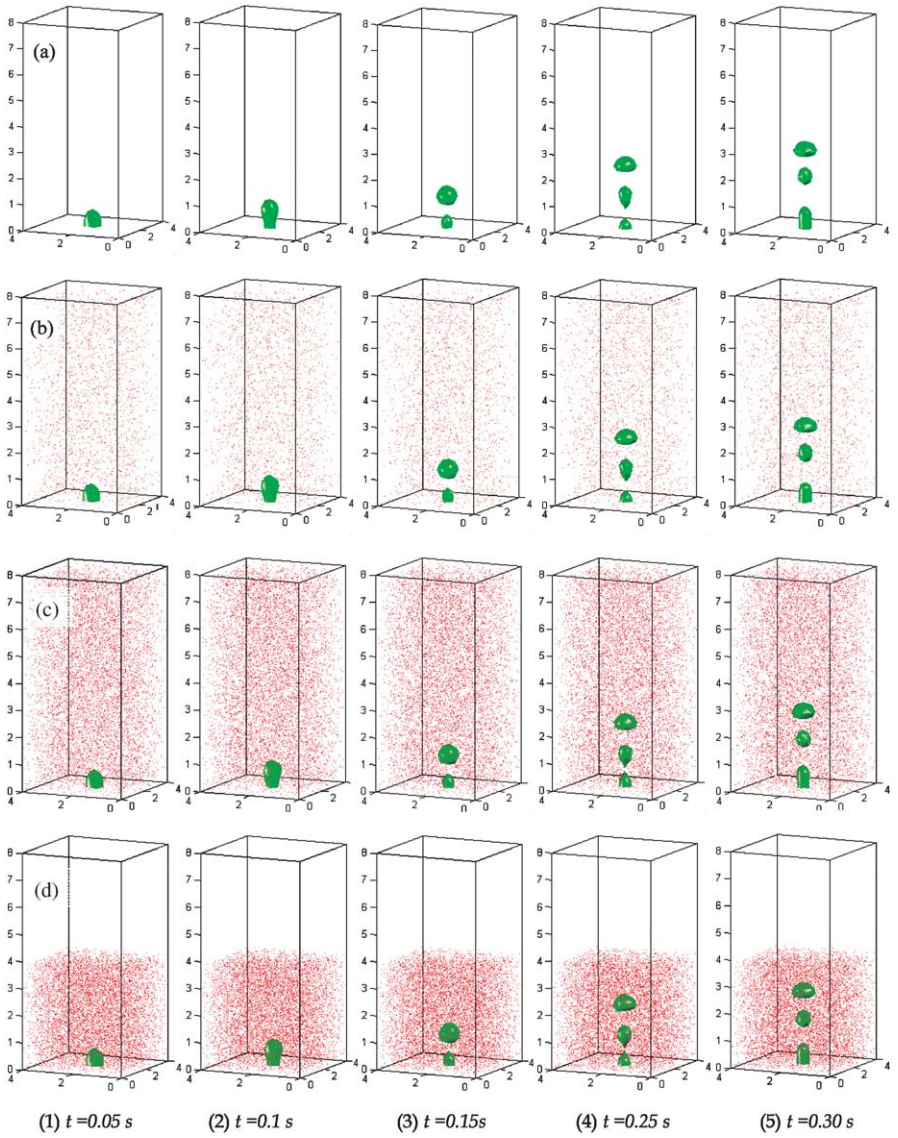

FIG. 7. Simulation results of bubble formation and rising in Paratherm NF heat-transfer fluid with and without particles. Nozzle size 0.4 cm I.D., liquid velocity 0 cm/s, gas velocity 10 cm/s, and particle density 0.896 g/cm^3. (a) No particle; (b) 2000 particles; (c) 8000 particles; (d) 8000 particles.

for the three solids concentrations used in this simulation. After 0.4 s, however, significant changes can be found for the cases with high solids concentrations. This can be seen from the first bubble in each case. When the solid concentration is low or no solids are present, the first bubble grows on the

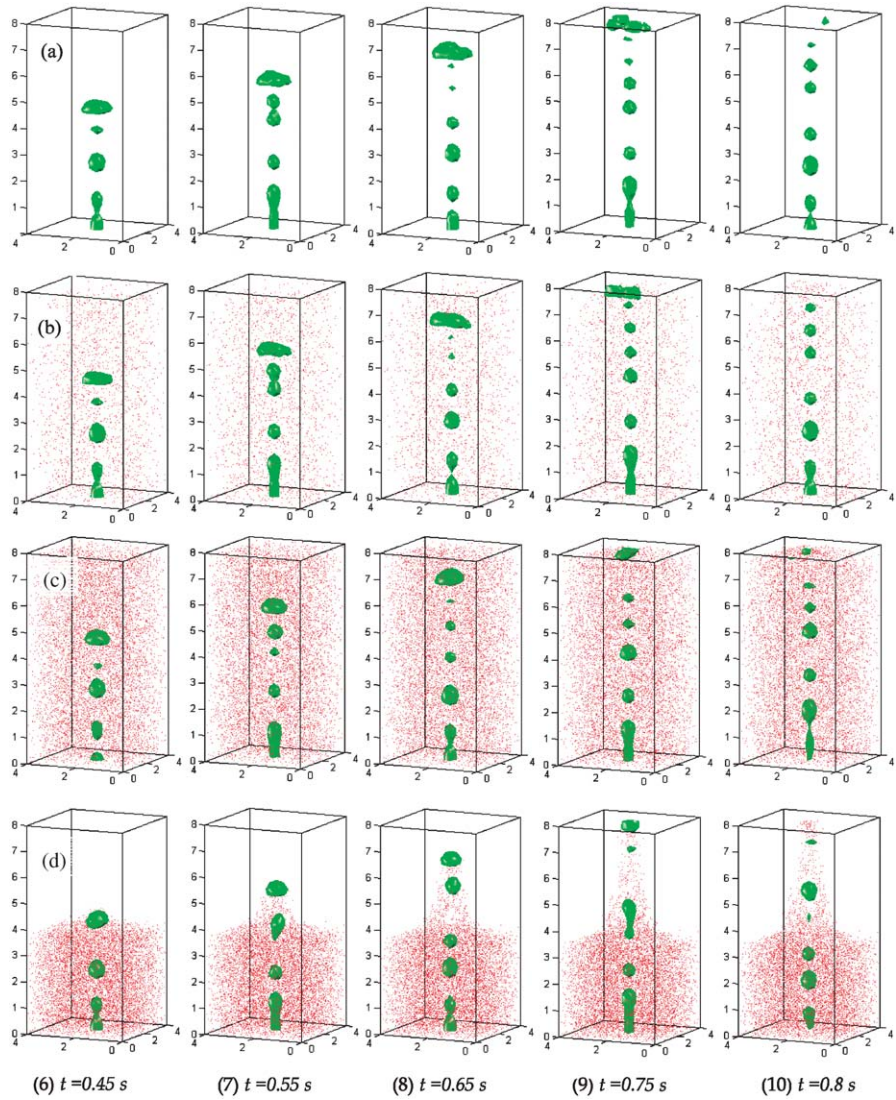

FIG. 7 (Continued)

orifice and connects to the second bubble. For the high solids concentration cases, the first bubble is not well connected to the second bubble. This is particularly true for Case (d) when the bubble rises into the solids-free region or freeboard region of the bed. The solid particle entrainment is clearly observed in Case (d).

IV. System 2: Deformation Dynamics of Liquid Droplet in Collision with a Particle with Film-Boiling Evaporation

The phenomena of evaporative liquid droplets impacting onto solid objects at high temperatures are of relevance to many engineering problems, such as sprinkler systems in the iron making or metal-casting processes, ink-jet spray-painting, impingement of oil droplets on turbine engines, meteorology, and spray coating of substrates. An evaporative liquid jet in gas–solid flow systems is also of interest to current technology applications in chemical, petroleum, and materials processing industries, such as FCC, polyethylene synthesis (Kunii and Levenspiel, 1991; Fan *et al.*, 2001) and microelectronic materials manufacturing. In FCC riser reactors, for example, gas oil at a low temperature is injected into the riser from feed nozzles located at the bottom of the riser and the mist droplets formed from the spray contact with high-temperature fluidized catalyst particles. The vaporized oil then carries the catalyst particle up through the riser. In the feed nozzle region, the size of the droplet can be comparable or significantly smaller (or larger) than the size of particle. The droplet can always have a different momentum, thus the collision between the catalytic particles and oil droplet may have various modes. Fig. 8 shows some of the collision modes existing in a feed-nozzle region (Zhu *et al.*, 2000). Smaller droplets may rebound from the surface of larger particles upon impact, and smaller particles

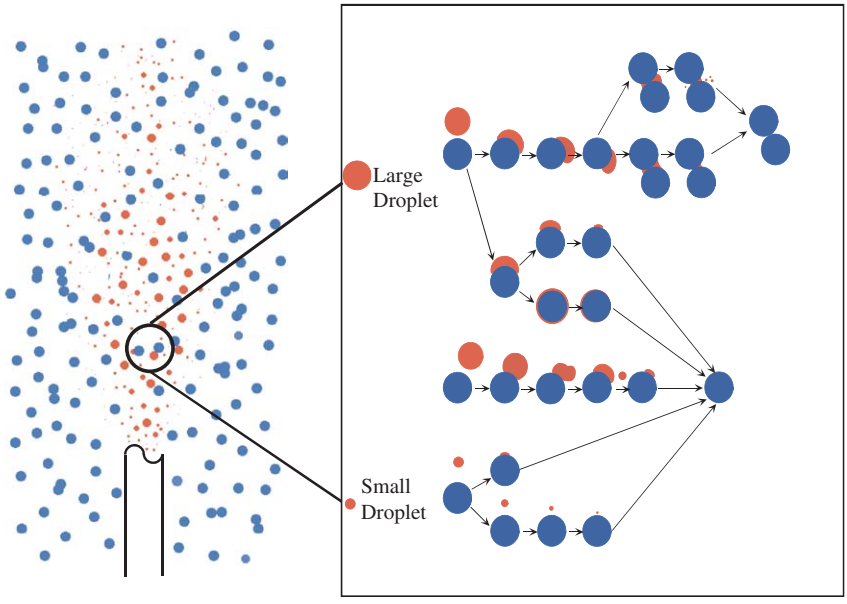

FIG. 8. Various modes of droplet–particle collisions.

may penetrate through or penetrate but retain inside the larger droplets. Larger droplets may break into smaller drops during the impact and/or remain attached to the particle surface after the collision, which may intensify the particle aggregation. Clearly, understanding the droplet and particle collision mechanics are crucial to an accurate account of the momentum and heat transfer between the droplet and solid object, which is important for prediction of hydrocarbon product distributions in light of catalytic and the thermal-cracking reactions in the riser. It is also relevant to the design of feed nozzles that provide desired droplet properties for optimum droplet contact with catalyst particles in the reactor.

In most of the applications, the solid objects (e.g., the catalyst particles in FCC reactor) are always under high temperature, and the droplet impact processes are accompanied with intensive evaporation. The nature of the collision of the droplet with the superheated objects exhibits a great diversity in hydrodynamic and thermodynamic properties, such as droplet splash and rebound, wetting or nonwetting contact, nucleate boiling or film boiling, and Marangoni effect. Further, the droplet shape, the contact area and the cooling effectiveness during the impact not only depend on such hydrodynamic forces as the inertia, pressure, surface tension, and viscous forces but also on the degrees of the surface superheating and the droplet subcooling (Inada *et al*., 1985). As the solid temperature rises to superheated conditions, the characteristics of liquid–solid contact significantly change and the evaporation rate affects the droplet hydrodynamics. Under this condition, the nonwetting contact may develop during the collision, and the evaporation is under the film-boiling regime, or so called Leidenfrost regime (Gottfried *et al*., 1966). In the Leidenfrost regime, the vapor pressure generated from the droplet evaporation prevents the direct contact of the droplet with the solid objects. The heat transfer from the hot objects to the droplet is also hindered due to the resistance of the vapor layer existing between the droplet and the solid surface. In this work, a 3-D numerical model is developed and the simulation is conducted to account for the behavior of the droplet–particle collision in the Leidenfrost regime.

Experimental and numerical studies of droplets impacting onto a flat surface of varied temperatures have been extensively reported in the literature. The effects of the initial droplet temperature on film-boiling impact are significant (Inada *et al*., 1985; Harvie and Fletcher, 2001b). Depending on the initial droplet temperature, there are two types of droplet impact: saturated impact and subcooled impact. The saturated impact involves the initial temperature at the boiling point of the liquid or saturation temperature of the liquid. The subcooled impacts, on the other hand, involve the droplet initial impact temperature below the liquid-saturation temperature. The experimental results for these two types of impact are briefly described below. The modeling and numerical approaches used for the droplet impingement onto isothermal or heated flat wall are also given.

A. Simulation of Saturated Droplet Impact on Flat Surface in the Leidenfrost Regime

Wachters and Westerling (1966) first presented a classification of the dynamic regimes of the impact based on their experiments in which water drops with a diameter of 2.3 mm impact on a polished gold surface at temperatures between 200 °C and 400 °C. They studied the saturated impact of water droplets and found that for the impact with $We < 30$, where $We = 2\rho_l V^2 R/\sigma$, the surface tension of the droplet dominates the impact process, and the droplet recoils and rebounds from the surface without disintegration. At $30 < We < 80$, the droplet undergoes a similar spreading and recoiling process as that for $We < 30$. In the rebounding process, the droplet may disintegrate into several smaller droplets (secondary droplets) and the shape of the droplet may then become unstable. For the impact with $We > 80$, the impact inertial force (or kinetic energy) is so large that splashing occurs during the early stage of the impact, while the droplet breaks up into a number of small droplets. Based on the measured heat flux on the solid surface, Wachters and Westerling (1966) also estimated the relative volume decrease of the droplet during the impact. It was found that, when the solid temperature is higher than 200 °C, the averaged evaporation rate of the droplet decreases with an increase in the surface temperature. At the nonwetting condition when the surface temperature reaches 400 °C, the volume (mass) change of the droplet due to the evaporation during the impact is slight (0.2–0.3%) for a wide range of We.

Groendes and Mesler (1982) studied the saturated film boiling impacts of a 4.7 mm water droplet on a quartz surface of 460 °C. The fluctuation of the surface temperature was detected using a fast-response thermometer. The maximal temperature drop of the solid surface during a droplet impact was reported to be about 20 °C. Considering the lower thermal diffusivity of quartz, this temperature drop implies a low heat-transfer rate on the surface. Biance *et al.* (2003) studied the steady-state evaporation of the water droplet on a superheated surface and found that for the nonwetting contact condition, the droplet size cannot exceed the capillary length.

Ge and Fan (2005) developed a 3-D numerical model based on the level-set method and finite-volume technique to simulate the saturated droplet impact on a superheated flat surface. A 2-D vapor-flow model was coupled with the heat-transfer model to account for the vapor-flow dynamics caused by the Leidenfrost evaporation. The droplet is assumed to be spherical before the collision and the liquid is assumed to be incompressible.

1. Hydrodynamic Model and Numerical Solution

In the level-set method, the free surface of the droplet is taken as the zero in the level-set function $\phi(\vec{x}, t)$ as given in Eq. (2). The motion of the interface is

traced by solving the Hamilton–Jacobi-type convection equation, given as Eq. (3), in the computational domain. The mass loss of the droplet due to evaporation during the impact process is neglected in surface-tracking based on the experimental results of Wachters and Westerling (1966). With the level-set method, the equation of motion of the fluid follows the Navier–Stokes equation as given by Eqs. (5) and (6). The density and viscosity are defined by Eqs. (10) and (11).

The computational code used in solving the hydrodynamic equation is developed based on the CFDLIB, a finite-volume hydro-code using a common data structure and a common numerical method (Kashiwa *et al.*, 1994). An explicit time-marching, cell-centered Implicit Continuous-fluid Eulerian (ICE) numerical technique is employed to solve the governing equations (Amsden and Harlow, 1968). The computation cycle is split to two distinct phases: a Lagrangian phase and a remapping phase, in which the Arbitrary Lagrangian Eulerian (ALE) technique is applied to support the arbitrary mesh motion with fluid flow.

Let $\phi^n = \phi(\vec{x}, t^n)$ and $\vec{V}^n = \vec{V}(\vec{x}, t^n)$ be the cell-centered level-set function and velocity at time t^n, respectively. The numerical procedures to solve the velocity field $\vec{V}^{n+1}$, and the level-set function ϕ^{n+1} at $t^{n+1} = t^n + \Delta t$ can be described below:

(1) Compute the velocity field $\vec{V}^{n+1}$ by solving the governing equation, Eqs. (5–6), using the cell-centered ICE technique and ALE technique (Kashiwa *et al.*, 1994).
(2) Solve the convection equation of $\phi(\vec{x}, t)$ (Eq. (3)) to obtain the $\bar{\phi}^{n+1}$. The high order (3rd order) essentially non-oscillatory (ENO) upwind scheme (Sussman *et al.*, 1994) is used to calculate the convective term $\vec{V}_\Gamma \cdot \nabla\phi$ based on the updated velocity field $\vec{V}^{n+1}$. The time advancement is accomplished using the second-order total variation diminishing (TVD) Runge-Kutta method (Chen and Fan, 2004).
(3) Perform the redistance procedure to obtain the ϕ^{n+1} using $\bar{\phi}^{n+1}$ as the initial value. The detail of the redistance computation is given by Sussman *et al.* (1998).
(4) Calculate the density and the viscosity of the field using Eqs. (10)–(11) with the updated level-set function ϕ^{n+1}.

The time steps (Δt) for calculating the $\vec{V}^{n+1}$ and the ϕ^{n+1} are the same, which is determined by the CFL condition and under constraints of the viscous and surface tension (Sussman *et al.*, 1994).

Considering a surface temperature which is higher than the Leidenfrost temperature of the liquid in this study, it is assumed that there exists a microscale vapor layer which prevents a direct contact of the droplet and the surface. Similar to Fujimoto and Hatta (1996), the no-slip boundary condition is adopted at the solid surface during the droplet-spreading process and the free-slip

condition is applied for the recoiling and rebounding periods. The velocity at the grid point inside the solid surface is solved together with whole domain but is reset according to the relative boundary condition (Ge and Fan, 2005).

2. *Vapor-Flow Model*

As the thickness of the vapor layer (5–20 μm) is several orders of magnitude smaller than the macroscale of the flow field (i.e., the diameter of the droplet), it would be impractical to use the same computation mesh for both macroflow and vapor-layer flow (Harvie and Fletcher, 2001a). Thus, a 2-D model is developed to simulate the dynamics of the vapor flow between the droplet and the surface. For the film-boiling impact problem, the vapor-layer model would allow determination of the evaporation-induced pressure in the vapor layer without neglecting the inertial force of the vapor flow. In the symmetrical coordinates (ξ,λ) shown in Fig. 9, assuming that the gas in the vapor layer is only saturated vapor and neglecting the temporal term, the continuity and momentum equations for incompressible vapor flows with gravitation terms neglected are given by

$$\frac{\partial u_\xi}{\partial \xi} + \frac{u_\xi}{\xi} + \frac{\partial u_\lambda}{\partial \lambda} = 0 \tag{43}$$

$$u_\xi \frac{\partial u_\xi}{\partial \xi} + u_\lambda \frac{\partial u_\xi}{\partial \lambda} = -\frac{\partial}{\partial \xi}\left(\frac{P}{\rho}\right) + v\left(\frac{\partial^2 u_\xi}{\partial \lambda^2} - \frac{\partial^2 u_\lambda}{\partial \xi \partial \lambda}\right) \tag{44}$$

$$u_\xi \frac{\partial u_\lambda}{\partial \xi} + u_\lambda \frac{\partial u_\lambda}{\partial \lambda} = -\frac{\partial}{\partial \lambda}\left(\frac{P}{\rho}\right) + v\left(\frac{\partial^2 u_\lambda}{\partial \xi^2} - \frac{\partial^2 u_\xi}{\partial \xi \partial \lambda} + \frac{1}{\xi}\frac{\partial u_\lambda}{\partial \xi} - \frac{1}{\xi}\frac{\partial u_\xi}{\partial \lambda}\right) \tag{45}$$

where u_ξ, u_λ are the vapor-flow velocities in ξ and λ direction, respectively, v is the kinematical viscosity of the vapor. To determine the relative significance of

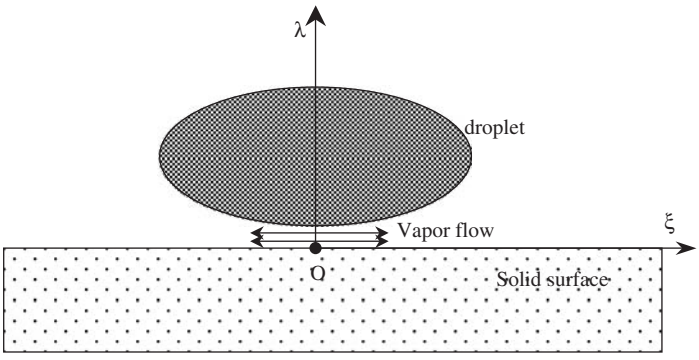

FIG. 9. Coordinates for the vapor-layer model.

each term in these motion equations, an order of magnitude analysis is made by considering the following dimensionless groups:

$$\bar{\xi} = \frac{\xi}{R}, \quad \eta = \frac{\lambda}{\delta}, \quad \bar{u}_\xi = \frac{u_\xi}{U_\xi}, \quad \bar{u}_\lambda = \frac{u_\lambda}{U_\lambda}, \quad \bar{p} = \frac{p}{\rho U_\xi^2}, \quad \bar{t} = \frac{tU_\xi}{R}, \quad Re_\delta = \frac{\delta(\xi)u_{\lambda\delta}}{\nu} \tag{46}$$

where R is the droplet radius; δ the vapor-layer thickness; Re_δ the local evaporation Reynolds number; $u_{\lambda\delta}(\xi)$ the local vapor velocity; and U_ξ, U_λ the velocity scalars in ξ, λ directions, respectively. Two assumptions can be made in accounting for the collision process: (a) The vapor-layer thickness is much smaller than the radius of the droplet; (b) The velocity for the vapor flow is much larger than the rates of variation of the vapor-layer thickness and breadth. Based on these assumptions and the order of magnitude analysis, the ξ momentum equation can be simplified to:

$$u_\xi \frac{\partial u_\xi}{\partial \xi} + u_\lambda \frac{\partial u_\xi}{\partial \lambda} = -\frac{\partial}{\partial \xi}\left(\frac{P}{\rho}\right) + \nu \frac{\partial^2 u_\xi}{\partial \lambda^2} \tag{47}$$

The boundary conditions are:

$$\begin{gathered} \lambda = 0, \quad u_\xi(\xi, 0) = u_\lambda(\xi, 0) = 0 \\ \lambda = \delta, \quad u_\xi(\xi, \delta) = u_l(\xi), \quad u_\lambda(\xi, \delta) = u_{\lambda\delta}(\xi) \\ \xi = 0, \quad \tfrac{\partial}{\partial \xi} = 0; \quad \xi = \xi_b, \; p = p_\mathrm{b} \end{gathered} \tag{48}$$

where p_b is the pressure of the ambient gas at the outside edge of the vapor layer.

In the impact process that involves large temperature differences (ΔT) between the surface and the droplet, such as the ones considered in this study (e.g., $\Delta T \cong 300$–$500\,^\circ\mathrm{C}$), the value for Re_δ is about 0.5–1.0. Thus, the inertial force of the vapor flow would be of the same order of magnitude as the viscous force, and cannot be neglected in Eq. (47) for the vapor-flow model.

To solve Eq. (47), a variable transformation is considered:

$$u_\lambda(\xi, \eta) = -\eta u_{\lambda\delta}(\xi) \quad u_\xi(\xi, \eta) = \Omega(\xi)\Phi(\eta) \tag{49}$$

$u_{\lambda\delta}$ (ξ) can be calculated through the energy-balance equation at the vapor–droplet interface. Ω(ξ) and Φ(η) are single-variable functions.

With this transformation, the solution for the ξ momentum can be converted into that of an ordinary differential equation (ODE) of $\Omega(\xi)$:

$$\Phi''(\eta) + Re_\delta \eta \Phi'(\eta) - Re_\delta \Phi(\eta) = \varphi(\xi) \tag{50}$$

$$\varphi(\xi) = \frac{\delta^2}{\nu \Omega(\xi)} \frac{\partial}{\partial \xi}(P/\rho) \tag{51}$$

The general solution of the Eq. (50) can be obtained in power series form. Under the condition that $Re_\delta \leq O(1)$, $\Phi(\eta)$ can be approximated by only including the first three terms in the power series with good accuracy:

$$\Phi(\eta) = \Phi_\delta \eta - \varphi(\xi)\eta\left(\frac{1}{2} - \frac{Re_\delta}{24}\right) + \varphi(x)\left(\frac{\eta^2}{2} - \frac{Re_\delta}{24}\eta^4\right) \tag{52}$$

The averaged vapor-flow velocity is given by

$$\bar{u}_\xi(\xi) = \Omega \int_0^1 \Phi_\delta \mathrm{d}\eta = \frac{1}{2}u_{l\delta}(\xi) - \frac{\delta^2}{12\gamma}\left(1 - \frac{3}{20}Re_\delta\right)\frac{\partial}{\partial\xi}\left(\frac{p}{\rho}\right) \tag{53}$$

The vapor-continuity equation can be expressed by

$$\bar{u}_\xi(\xi) = \frac{1}{\xi\delta(\xi)}\int_0^\xi \xi' u_{\lambda\delta}(\xi')\mathrm{d}\xi' \tag{54}$$

The pressure distribution in the vapor layer can be obtained by solving Eqs. (53) and (54) using a piecewise integration method (Ge and Fan, 2005). In this procedure, the thickness of the vapor layer $\delta(\xi)$ is obtained from the level-set function. The $u_{\lambda\delta}(\xi)$ is calculated by

$$u_{\lambda\delta}(\xi) = \dot{m}/\rho_v - \frac{\partial\delta(\xi)}{\partial t} \tag{55}$$

where the local evaporation rate $\dot{m}$ is defined by the heat-transfer model. The vapor-pressure force simulated by this model is applied as an interfacial force to the droplet bottom surface.

3. *Heat-Transfer Model*

Heat transfer occurs not only within the solid surface, droplet and vapor phases, but also at the liquid–solid and solid–vapor interface. Thus, the energy-balance equations for all phases and interfaces are solved to determine the heat-transfer rate and evaporation rate.

Inside the solid surface, the heat-conduction equation in 3-D coordinates is

$$\frac{\partial T_s}{\partial t} = \alpha_s\left(\frac{\partial}{\partial x}\left(\frac{\partial T_s}{\partial x}\right) + \frac{\partial}{\partial y}\left(\frac{\partial T_s}{\partial y}\right) + \frac{\partial}{\partial z}\left(\frac{\partial T_s}{\partial z}\right)\right) \tag{56}$$

where $T_s(x,y,z)$ is the solid temperature and α_s the thermal diffusivity of solid. The heat transfer within the droplet is described by the following thermal-energy transport equation with neglecting viscous dissipation:

$$\frac{\partial T_\mathrm{d}}{\partial t} + u\frac{\partial T_\mathrm{d}}{\partial x} + v\frac{\partial T_\mathrm{d}}{\partial y} + w\frac{\partial T_\mathrm{d}}{\partial z} = \alpha_\mathrm{d}\left(\frac{\partial^2 T_\mathrm{d}}{\partial x^2} + \frac{\partial^2 T_\mathrm{d}}{\partial y^2} + \frac{\partial^2 T_\mathrm{d}}{\partial z^2}\right) \tag{57}$$

Using the same assumptions that were made in the vapor-layer model, the energy-conservation equation for the incompressible 2-D vapor phase can be simplified to a 1-D equation in boundary layer coordinates:

$$\frac{\partial^2 T_v}{\partial \eta^2} = 0 \tag{58}$$

The radiative heat transfer across the vapor layer is neglected under the condition that the solid temperature is lower than 700 °C (Harvie and Fletcher, 2001a,b). On the liquid–vapor interface, the energy-balance equation is

$$k_{\mathrm{v}} \frac{T_{\mathrm{ss}} - T_{\mathrm{ds}}}{\delta} = \dot{m} L_{\mathrm{c}} \tag{59}$$

where k_{v} is the thermal conductivity of the vapor; T_{ss} and T_{ds} are the temperatures of the solid surface and the droplet surface. The thermal boundary condition at the solid–vapor interface is

$$k_{\mathrm{v}} \frac{T_{\mathrm{ss}} - T_{\mathrm{ds}}}{\delta} = -k_{\mathrm{s}} \frac{\partial T_{\mathrm{s}}}{\partial \eta} \tag{60}$$

where the heat flux in the η direction is assumed to be much larger that that in the ξ direction.

The numerical method used for solving the heat-transfer equation is similar to that for solving the momentum equation, which is a finite-volume, ALE method (Kashiwa *et al.*, 1994).

4. *Results and Discussion*

To validate the model developed in the present study, the simulations are first conducted and compared with the experimental results of Wachters and Westerling (1966). In their experiments, water droplets impact in the normal direction onto a hot polished gold surface with an initial temperature of 400 °C. Different impact velocities were applied in the experiment to test the effect of the *We* number on the hydrodynamics of the impact. The simulation of this study is conducted for cases with different Weber numbers, which represent distinct dynamic regimes.

The simulation shown in Fig. 10 is an impact of a saturated water droplet of 2.3 mm in diameter onto a surface of 400°C with an impact velocity of 65 cm/s, corresponding to a Weber number of 15. This simulation and all others presented in this study are conducted on uniform meshes ($\Delta x = \Delta y = \Delta z = \Delta$). The mesh resolution of the simulation shown in Fig. 10 was 0.08 mm in grid size, although different resolutions are also tested and the results are compared in Figs. 11 and 12. The average time-step in this case is around 5 μs. It takes 4000 iterations to simulate a real time of 20 ms of the impact process. The simulation

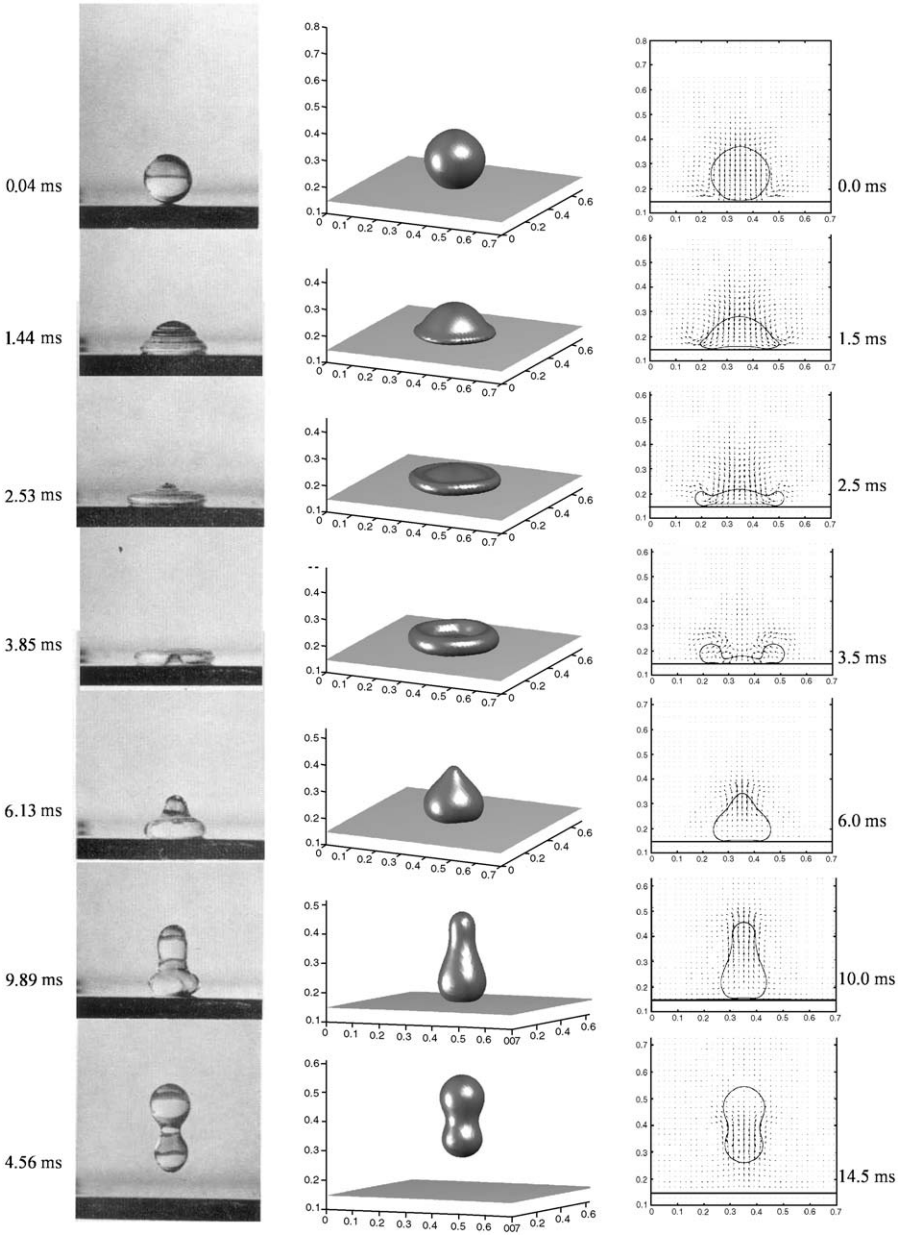

FIG. 10. Water droplet impacts on a flat surface. The initial droplet diameter is 2.3 mm and the surface temperature is 400 °C. $We = 15$.

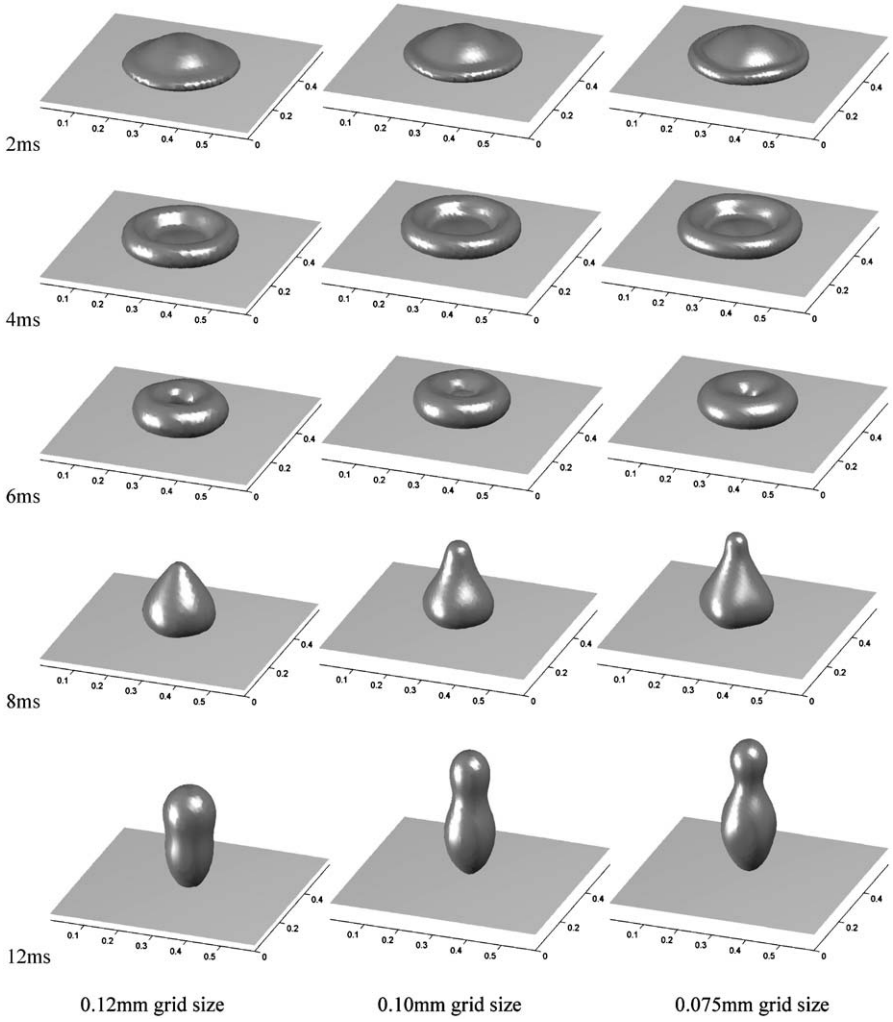

FIG. 11. Simulated 3-D views of the impact for $We = 15$ as a function of the mesh resolution.

code is run on the cray-SV1 supercomputer at the OSC. The computing time of this case is about 12 h.

Comparing the 3-D images simulated and the experimental photographs in Fig. 10, it can be seen that the droplet shapes are well reproduced by the present model. During the first 3.5 ms of the impact (frames 1–3), a liquid film with flattened disc shape is formed immediately after the impact. The inertial force drives the liquid to continue spreading on the solid surface, while the surface tension and the viscous forces resist the spreading of the liquid film. As a result, the droplet spreading speed decreases and the fluid mass starts to accumulate at

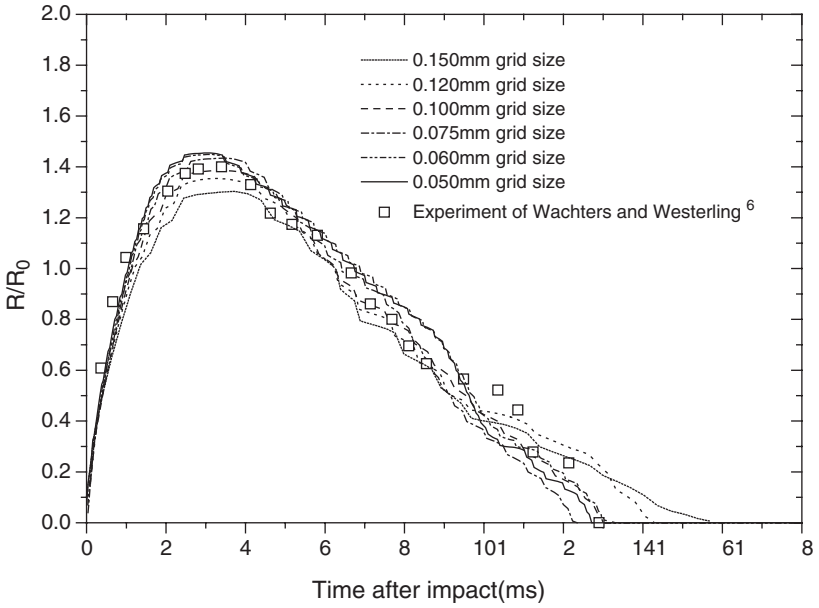

FIG. 12. Spread factor of the droplet verse time for the impact condition given in Fig. 10 at different mesh resolutions.

the leading edge of the liquid film (2.5–3.2 ms). After the droplet spreads to the maximum extent, the liquid film starts to shrink back to its center (frames 4 and 5) due to the surface-tension force at the edge of the film. At 3.55 ms (frame 4), the simulated droplet shows a concave structure with a void in the center, which is also shown in the experimental photograph of 3.85 ms. This structure, also called a ring structure, has also been widely reported in the literature. In the cross-sectional images at 3.55 ms, the velocity field shows that the inward flow first starts from the outer edge of the liquid film, which confirms that recoiling flow is driven by the surface tension. After 4.4 ms, the droplet continues to recoil and forms an upward flow in the center of the droplet (frames 5 and 6), and this leads to a bouncing of the droplet up from the surface (frame 7). The peanut-shape droplet (also called dumb-bell shape by Harvie and Fletcher (2001b) shown in the experimental photograph at 14.56 ms is reproduced in the simulation.

The impact process shown in Fig. 10 is also simulated at six different grid resolutions, i.e., 0.150, 0.120, 0.100, 0.075, 0.060, and 0.050 mm in mesh sizes, with the corresponding cells per droplet radius (CPR) of 7.6, 9.6, 11.5, 15.3, 19.0, and 23.0, respectively. The comparison of the 3-D images among three resolutions is shown in Fig. 11. The corresponding CPRs of these resolutions are 9.6, 11.5, and 15.3. It can be found that the simulated droplet shapes are similar at all three resolutions during the spreading process and even the early stage of the recoiling process (2–6 ms). The deviation appears in the late stage of

the recoiling process (8 ms), while the droplet generated on coarser mesh (0.12 mm) tends to be more uniform in structure and less elongated in the vertical direction. The difference in the droplet shape for 0.1 mm mesh and 0.075 mm mesh is relatively small.

Fig. 12 shows the spread factors simulated on meshes with different resolutions along with the measurement value of Wachters and Westerling (1966). The spread factor is defined as the radius of the droplet on the solid surface divided by the initial radius of the droplet. Although the convergence is not perfect, the agreement between the experiment and the simulations is relatively good for all resolutions. Consistent with the results of Fig. 11, the effect of the mesh resolution on spread factor becomes notable after 8 ms since the moment of impact, and the coarser resolution tends to yield a slower rebounding process.

The simulations were also performed under same conditions as the case of Fig. 10 but for higher impact velocities. The simulated-droplet dynamics and heat-transfer rate at the solid surface at different impact velocities are given in Ge and Fan (2005).

B. Simulation of Subcooled Droplet Impact on Flat Surface in Leidenfrost Regime

Subcooled impacts, in which the initial temperature of the droplet is below the liquid saturation temperature, are of primary interest in experiments since the condition of the spray liquids is often of the ambient temperature in practical applications (Inada *et al.*, 1985; Chandra and Avedisian, 1991; Chen and Hsu, 1995). Chandra and Avedisian (1991) studied the collision dynamics of a 24 °C *n*-heptane droplet impacting on a metallic surface with a Weber number equal to 43. The transition from the nucleate boiling to the film boiling was identified when the surface temperature rises from the boiling point (170 °C) to above the Leidenfrost temperature (200 °C) of *n*-heptane. They found that under the film-boiling condition, the liquid–solid contact is hindered by the vapor layer, as evidenced by the disappearance of the bubbles inside the liquid droplet under the nucleate boiling condition. The contact angle of the liquid to the surface was also reported to increase with an increase in the surface temperature, and reached 180° in the film boiling condition. Qiao and Chandra (1996) measured the temperature drop of a stainless steel surface during the impact of the subcooled water and the *n*-heptane droplets in low gravity. They found that when the surface temperature is above the superheat limit, the temperature drop of the surface is relatively small for the impact of *n*-heptane droplet (less than 20 °C). But for the impact of the water droplet, the temperature drop of the surface can reach 150 °C, which implies a high heat flux and the intermittent contact of the liquid and the solid surface. Hatta *et al.* (1997) found that at low impact *We* number, the dynamics of water droplet is almost independent of

the surface materials when the surface temperature is above the Leidenfrost temperature.

The effects of the subcooling degree of the droplet on the film-boiling impact are studied by Inada *et al.* (1985). They found that the heat-transfer rate on the solid surface during an impact of a 4-mm water droplet increases significantly with a decrease in the initial droplet temperature. The boiling regimes were classified to represent different droplet dynamics and heat-transfer modes at various droplet and surface temperatures. Inada *et al.* (1988) also measured the thickness of the vapor film between the impinging droplet and the surface at various degrees of subcooling. Chen and Hsu (1995) measured the transient local heat flux at the surface of a presuperheated plate, which undergoes the impingement of subcooled water droplets. A fast-response microthermocouple was designed to capture the instantaneous changes of the solid-surface temperature. Although the droplet dynamics of the impact process was not presented, they concluded that both the surface temperature and the degree of the droplet subcooling are crucial to the intermittent contact mode at the solid surface. At the film-boiling regime with the surface temperature superheated at 400 °C, a subcooled droplet tends to disintegrate during the impact at $We = 55$.

In subcooled impact, the initial droplet temperature is lower than the saturated temperature of the liquid of the droplet, thus the transient heat transfer inside the droplet needs to be considered. Since the thickness of the vapor layer may be comparable with the mean free path of the gas molecules in the subcooled impact, the kinetic slip treatment of the boundary condition needs to be applied at the liquid–vapor and vapor–solid interface to modify the continuum system.

1. Hydrodynamic Model

The flow field of the impacting droplet and its surrounding gas is simulated using a finite-volume solution of the governing equations in a 3-D Cartesian coordinate system. The level-set method is employed to simulate the movement and deformation of the free surface of the droplet during impact. The details of the hydrodynamic model and the numerical scheme are described in Sections II.A and 1 V.A.1.

During the subcooled droplet impact, the droplet temperature will undergo significant changes due to heat transfer from the hot surface. As the liquid properties such as density $\rho_l(T)$, viscosity $\mu_l(T)$, and surface tension $\sigma(T)$ vary with the local temperature T, the local liquid properties can be quantified once the local temperature can be accounted for. The droplet temperature is simulated by the following heat-transfer model and vapor-layer model. Since the liquid temperature changes from its initial temperature (usually room temperature) to the saturated temperature of the liquid during the impact, the linear

variation of liquid properties with the temperature is assumed, which is

$$\gamma(T) = \gamma_0 + \frac{T - T_0}{T_{sa} - T_0}(\gamma_{sa} - \gamma_0) \quad \gamma = \rho_l, \mu_l, \sigma \tag{61}$$

where T_0 and T_{sa} are the initial and saturated temperatures of the liquid respectively; γ_0 and γ_{sa} are the liquid property at T_0 and T_{sa}, respectively. The boundary condition adopted at the solid surface is described in Section IV.A.1.

2. Heat Transfer Inside the Droplet and Across the Vapor Layer

For the subcooling impact, especially for the high subcooling degree case in which the droplet initial temperature is much lower than the saturated temperature, the heat transfer within the droplet is significant and hence affects the droplet evaporation rate. Neglecting the viscous dissipation, the equation of the conservation of the thermal energy inside the droplet is given by

$$\frac{\partial T}{\partial t} + \vec{V} \cdot \nabla T = \alpha_l \nabla \cdot \nabla T \tag{62}$$

where α_l is the thermal diffusivity of liquid. At other free surfaces of the droplet, the adiabatic boundary condition is applied which is given by

$$\vec{n}_\Gamma \cdot \nabla_d T = 0 \tag{63}$$

where $\vec{n}_\Gamma$ is the normal vector of the droplet surface, which can be calculated based on the level-set function:

$$\vec{n}_\Gamma = \frac{\nabla \phi}{|\nabla \phi|} \tag{64}$$

$\nabla_d T$ is the temperature gradient which is evaluated only on the droplet side. The heat-conduction equation inside the solid surface is given in Section IV.A.3.

The heat transfer across the vapor layer and the temperature distribution in the solid, liquid, and vapor phases are shown in Fig. 13. In the subcooled impact, especially for a droplet of water, which has a larger latent heat, it has been reported that the thickness of the vapor layer can be very small and in some cases, the transient direct contact of the liquid and the solid surface may occur (Chen and Hsu, 1995). When the length scale of the vapor gap is comparable with the free path of the gas molecules, the kinetic slip treatment of the boundary condition needs to be undertaken to modify the continuum system. Consider the Knudsen number defined as the ratio of the average mean free path of the vapor to the thickness of the vapor layer:

$$Kn = \frac{\lambda}{\delta} \tag{65}$$

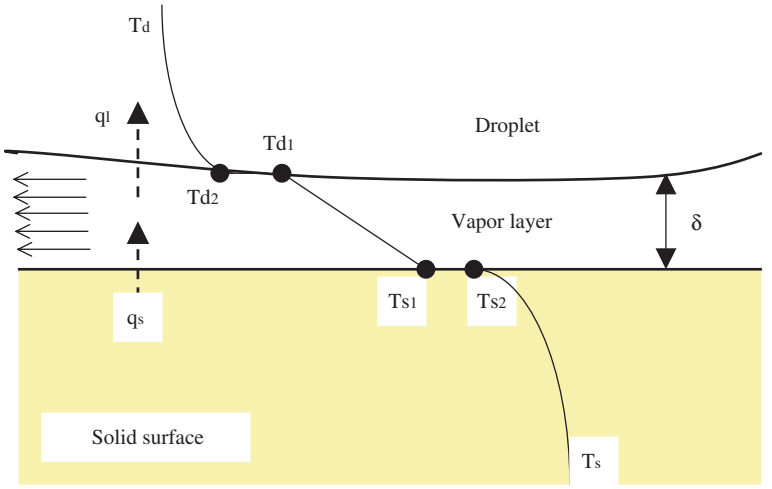

FIG. 13. Temperature distribution and heat flux across the vapor layer.

where λ is the mean free path of molecule. Harvie and Fletcher (2001c) analyzed the kinetic of the molecular behavior at the solid and evaporative surface for $0.01 < Kn < 0.1$. Based on their simple kinetic theory, the effective temperature discontinuity at liquid–vapor surface and solid–vapor surface can be given by

$$T_{s2} - T_{s1} = C_{T,s}(T_{s1} - T_{d2}) \tag{66}$$

$$T_{d1} - T_{d2} = C_{T,l}(T_{s1} - T_{d1}) \tag{67}$$

where $T_{s1}, T_{s2}, T_{d1}, T_{d2}$ are the interface temperatures of solid surface and droplet shown in Fig. 13. C_T is defined by

$$C_T = Kn\left(\frac{9}{4}\gamma - \frac{5}{4}\right)\left(\frac{2-\sigma_t}{\sigma_t}\right) \tag{68}$$

where σ_t is the thermal accommodation coefficient defined by Harvie and Fletcher (2001c). At the liquid–vapor interface, the energy balance equation is given by

$$k_v \frac{T_{s1} - T_{d1}}{\delta} = q_l + \dot{m}L_c \tag{69}$$

where k_v is the thermal conductivity of the vapor; L_c the latent heat of the liquid; q_l the heat flux at the droplet surface at the liquid side, which is given by $q_l = -k_l \nabla_d T$.

3. Vapor-Layer Model with Kinetic Treatment at Boundary

The vapor-layer model developed in Section IV.A.2 is based on the continuum assumption of the vapor flow. This assumption, however, needs to be modified by considering the kinetic slip at the boundary when the Knudsen number of the vapor is larger than 0.01 (Bird, 1976). With the assumption that the thickness of the vapor layer is much smaller than the radius of the droplet, the reduced continuity and momentum equations for incompressible vapor flows in the symmetrical coordinates (ξ,λ) are given as Eqs. (43) and (47). When the Knudsen number of the vapor flow is between 0.01 and 0.1, the flow is in the slip regime. In this regime, the flow can still be considered as a continuum at several mean free paths distance from the boundary, but an effective slip velocity needs to be used to describe the molecular interaction between the gas molecules and the boundary. Based on the simple kinetic analysis of vapor molecules near the interface (Harvie and Fletcher, 2001c), the boundary conditions of the vapor flow at the solid surface can be given by

$$\lambda = 0, \;\; u_\xi(\xi, 0) = F_\mathrm{s} \frac{\partial u_\xi}{\partial \lambda}(\xi, 0), \quad u_\lambda(\xi, 0) = 0 \tag{70}$$

and the boundary conditions at the droplet surface is

$$\lambda = \delta, \quad u_\xi(\xi, \delta) - u_{\xi,l}(\xi) = F_\mathrm{l} \frac{\partial \mathrm{u}_\xi}{\partial \lambda}(\xi, \delta), \; u_\lambda(\xi, \delta) = -u_{\lambda,l}(\xi) \tag{71}$$

where $u_{\xi,l}(\xi)$, $u_{\lambda,l}(\xi)$ are the velocities of the droplet surface in ξ and λ direction, respectively; F_s and F_l are defined by

$$F_\mathrm{s} = \lambda_\mathrm{s} \frac{2 - \sigma_{v,s}}{\sigma_{v,s}} \quad F_\mathrm{l} = \lambda_\mathrm{l} \frac{2 - \sigma_{v,l}}{\sigma_{v,l}} \tag{72}$$

where λ_s, λ_l are the mean free path of the gas molecules near solid and droplet surface.

Equations (43) and (47) can be solved by using the similar procedure as given by Section IV.A.2 with the boundary condition given by Eqs. (70) and (71). Thus the vapor pressure can be determined by

$$p(\xi) = p_0 + \int_\xi^{\xi_b} \rho \varphi(\xi) \, \mathrm{d}\xi \tag{73}$$

where ξ_0 is the radius of the extent of the vapor layer and$\varphi(r)$is given by

$$\varphi(\xi) = \frac{2\nu C_1}{\delta^2} \bar{u}_\xi - \frac{\bar{u}_\xi u_{\lambda l}}{\delta}(B_1 - B_2) + \frac{\bar{u}_\xi^2}{\xi} B_1 \tag{74}$$

where

$$
\begin{aligned}
B_1 &= \frac{C_1^2}{5} + \frac{C_1 C_2}{2} + \frac{2C_1 C_3 + C_2^2}{3} + C_1 C_3 + C_3^2 \\
B_2 &= \frac{2C_1^2}{15} + \frac{C_1 C_2}{3} + \frac{C_2^2}{6} + \frac{2}{3} C_1 C_3 + \frac{1}{2} C_2 C_3 \\
C_1 &= -3\frac{2 + 2k_l + 2k_s - \theta_l - 2k_s\theta_l}{1 + k_l + 4k_s + 6k_l k_s} \\
C_2 &= \frac{6 + 6k_l - 2\theta_l}{1 + k_l + 4k_s + 6k_l k_s} \\
C_3 &= k_s C_2
\end{aligned}
\tag{75}
$$

where $k_l = F_l/\delta, k_s = F_s/\delta, \theta_l = u_{\xi,l}/\bar{u}_\xi$.

The averaged velocity of the vapor is expressed by Eq. (54). The pressure distribution in the vapor layer can be obtained by solving Eqs. (54) and (73)–(75) by a piecewise integration method. Details of the solving procedure and how to use the vapor pressure in flow field calculation are given in Section IV.A.2.

4. *Results and Discussion*

Three different subcooled impact conditions under which experiments were conducted and reported in the literature are simulated in this study. They are: (1) *n*-heptane droplets (1.5 mm diameter) impacting on the stainless steel surface with $We = 43$ (Chandra and Avedisian, 1991), (2) 3.8 mm water droplets impacting on the inconel surface at a velocity of 1 m/s (Chen and Hsu, 1995), and (3) 4.0 mm water droplets impacting on the copper surface with $We = 25$ (Inada *et al.*, 1985). The simulations are conducted on uniform Cartesian meshes ($\Delta x = \Delta y = \Delta z = \Delta$). The mesh size (resolution) is determined by considering the mesh refinement criterion in Section V.A. The mesh sizes in this study are chosen to provide a resolution of CPR = 15.

Fig. 14 shows the comparison of the photographs from Chandra and Avedisian (1991) with simulated images of this study for a subcooled 1.5 mm *n*-heptane droplet impact onto a stainless-steel surface of 200 °C. The impact velocity is 93 cm/s, which gives a Weber number of 43 and a Reynolds number of 2300. The initial temperature of the droplet is room temperature (20 °C). In Fig. 14, it can be seen that the evolution of droplet shapes are well simulated by the computation. In the first 2.5 ms of the impact (frames 1–2), the droplet spreads out right after the impact, and a disk-like shape liquid film is formed on the surface. After the droplet reaches the maximum diameter at about 2.1 ms, the liquid film starts to retreat back to its center (frame 2 and 3) due to the surface-tension force induced from the periphery of the droplet. Beyond 6.0 ms, the droplet continues to recoil and forms an upward flow in the center of the

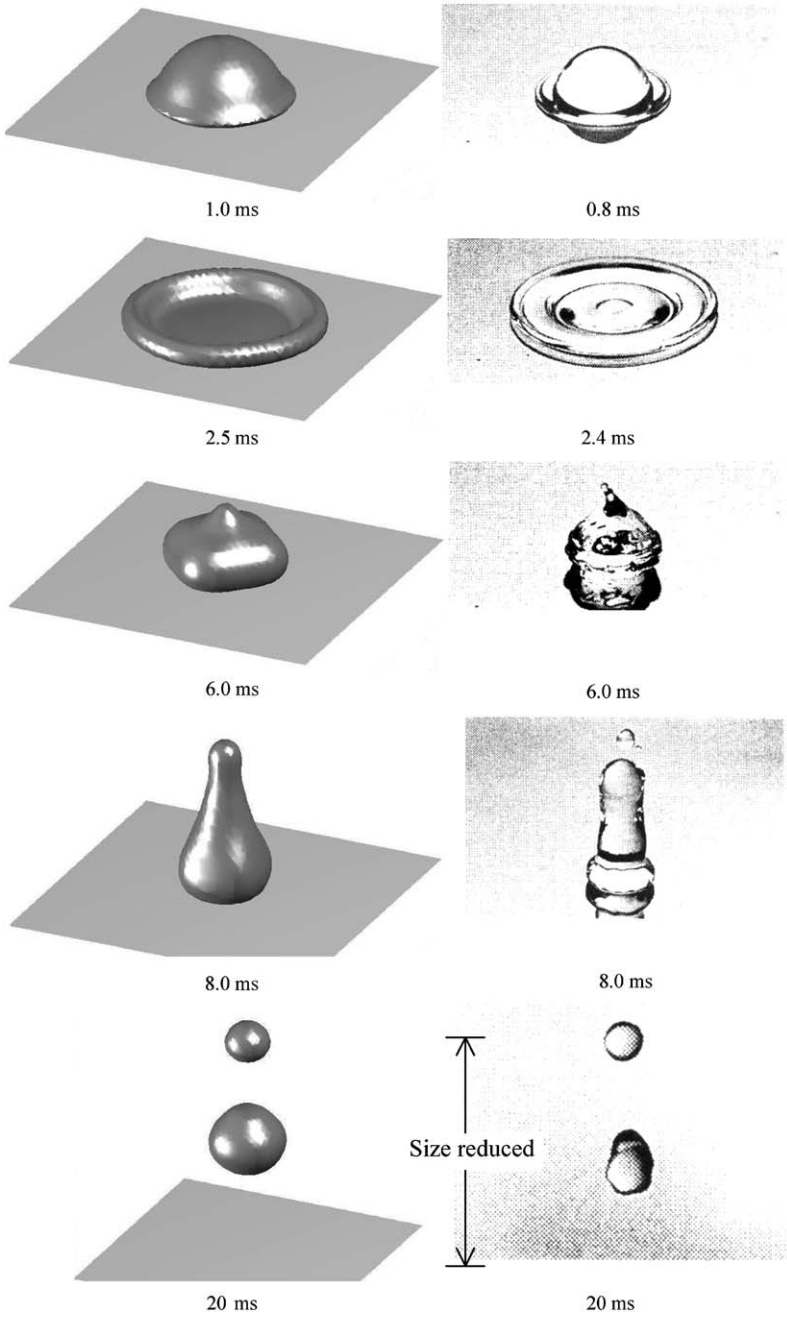

FIG. 14. *n*-Heptane droplet collision with surface at 200 °C. Experimental images (right) are presented by Chandra and Avedisian (1991). $We = 45$. The size of the last frame is reduced.

droplet (frames 3 and 4), which leads to the bouncing of the droplet up from the surface (frame 5). The photograph at 8.0 ms shows that the tip of the elongated droplet separates from the main body of the droplet and the main body of the droplet then breaks up into smaller secondary drops (frame 5). This phenomenon was reproduced accurately in the simulation.

Fig. 15 shows the detailed structure of the droplet from a viewing angle of 60°. Experimental images show that a hole is formed in the center of the droplet for a short time period (3.4–4.8 ms) and the center of the liquid droplet is a dry circular area. The simulation also shows this hole structure although a minor variation exists over the experimental images. As the temperature of the surface is above the Leidenfrost temperature of the liquid, the vapor layer between the droplet and the surface diminishes the liquid–solid contact and thus yields a low surface-friction effect on the outwardly spreading liquid flow. When the droplet periphery starts to retreat due to the surface-tension effect, the liquid in the droplet center still flows outward driven by the inertia, which leads to the formation of the hole structure.

The impact process of a 3.8 mm water droplet under the conditions experimentally studied by Chen and Hsu (1995) is simulated and the simulation results are shown in Figs. 16 and 17. Their experiments involve water-droplet impact on a heated Inconel plate with Ni coating. The surface temperature in this simulation is set as 400 °C with the initial temperature of the droplet given as 20 °C. The impact velocity is 100 cm/s, which gives a Weber number of 54. Fig. 16 shows the calculated temperature distributions within the droplet and within the solid surface. The isotherm corresponding to 21 °C is plotted inside the droplet to represent the extent of the thermal boundary layer of the droplet that is affected by the heating of the solid surface. It can be seen that, in the droplet spreading process (0–7.0 ms), the bulk of the liquid droplet remains at its initial temperature and the thermal boundary layer is very thin. As the liquid film spreads on the solid surface, the heat-transfer rate on the liquid side of the droplet–vapor interface can be evaluated by

$$q_{\text{drop}} = k_{\text{l}} \frac{T_{\text{d2}} - T_{\text{d,bulk}}}{\delta_{\text{T}}} \tag{76}$$

where δ_{T} is the thickness of the thermal boundary layer; T_{d2} and $T_{\text{d,bulk}}$ are the droplet temperature at the surface and in the bulk, respectively. The thermal boundary layer thickness can be estimated by (Pasandideh-Ford *et al.*, 2001):

$$\delta_{\text{T}} = \frac{2d_0}{Re^{0.5} Pr^{0.4}} \tag{77}$$

where Re is the Reynolds number of the impinging liquid flow and is defined by $Re = \rho V d_0/\mu$; and V the liquid film velocity. At the early stage of the spreading, V is close to the initial impact velocity of the droplet, and thus, it gives a thin thermal boundary layer as shown in frames 1 and 2 of Fig. 16. When

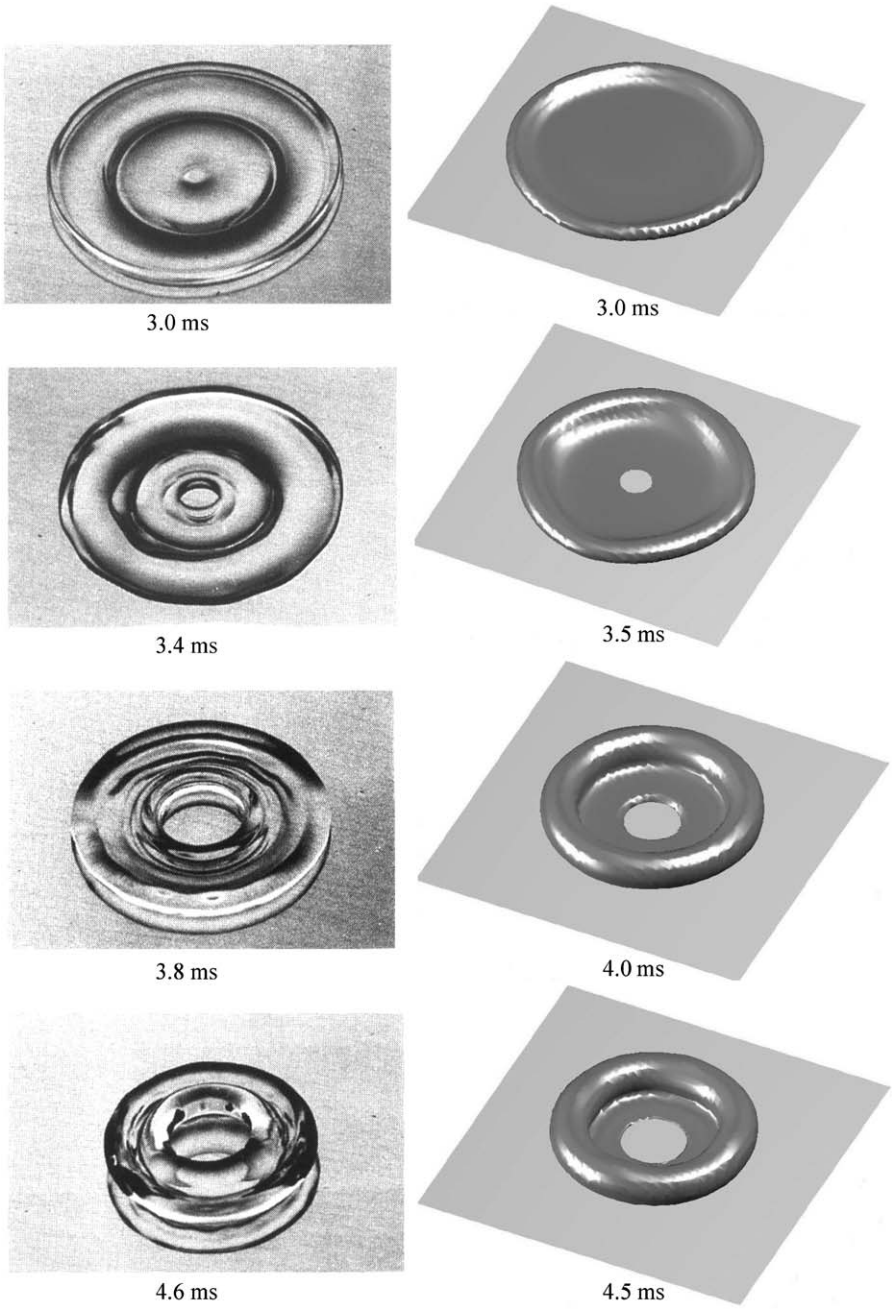

FIG. 15. Experimental photos (left) by Chandra and Avedisian (1991) and simulated images (right) of the spreading droplet on surface at 200 °C. The formation of a hole in the center of the liquid is captured.

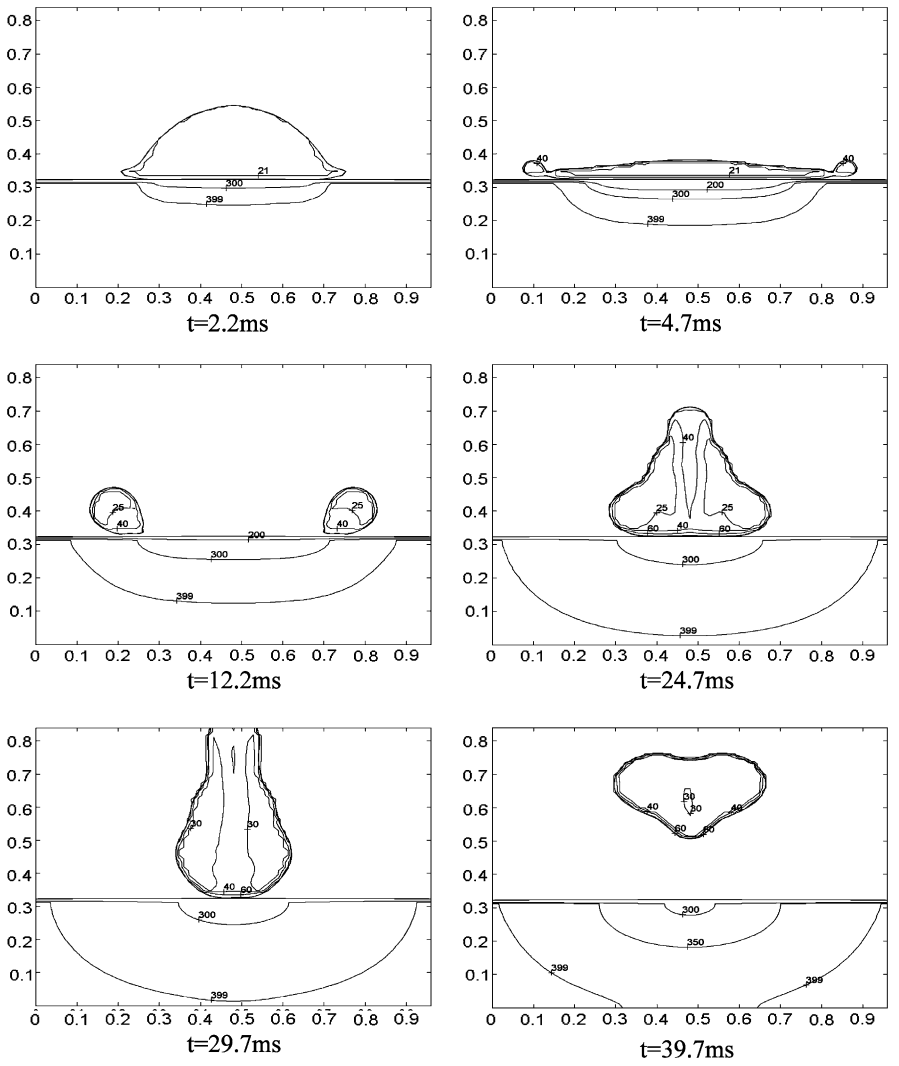

FIG. 16. Simulated temperature field in the liquid and solid phases.

the droplet spreads to the maximum extent and starts to recoil, the liquid velocity diminishes to zero and the thermal boundary layer is disrupted. Until then, the temperature rise inside the droplet becomes significant (frames 3 and 4 of Fig. 16). The simulated temperature distribution inside the solid surface is also shown in Fig. 16, in which the isotherm of 399 °C is chosen to represent the area of temperature drop during the impact of the droplet.

The simulation of droplet impact shown in Fig. 16 is conducted under perfectly symmetrical conditions, which is not easy to achieve in the experiments.

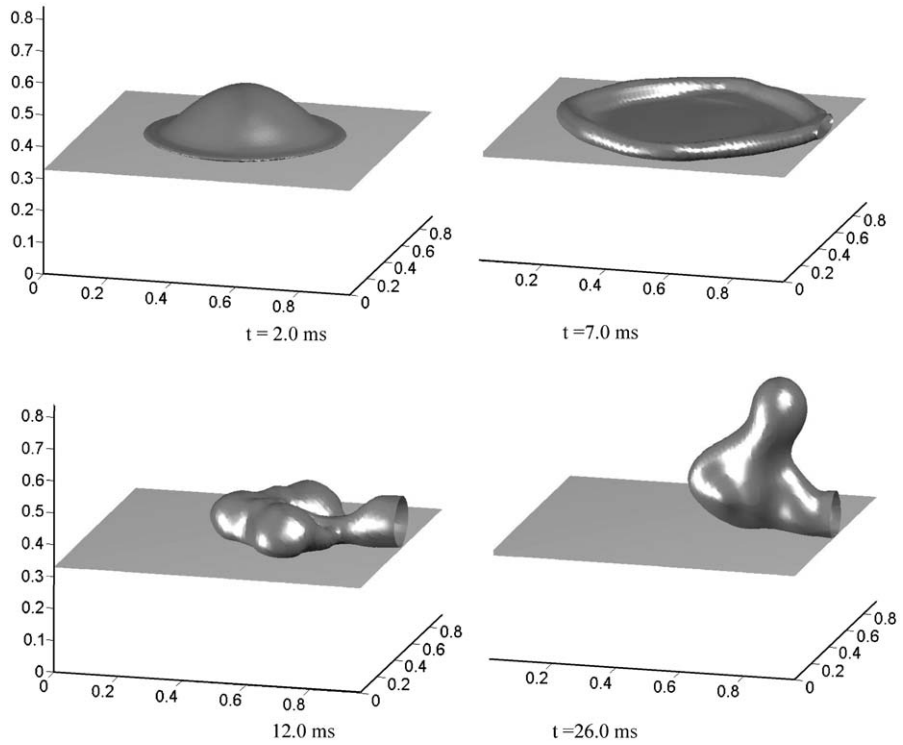

FIG. 17. Droplet impacts on the flat surface with a small tangential velocity. Other conditions are the same as those in Fig. 16.

As the droplet is released from the nozzle and moves toward the superheated surface, some uncontrollable factors such as the angle of dropping, obliquity of the surface, and perturbation in the ambient conditions render it difficult to maintain a perfectly normal collision between the droplet and solid surface. The 3-D simulation of this study is capable of reproducing the imperfect droplet–surface impact condition represented by asymmetrical collision. Fig. 17 shows the simulated 3-D images of the droplet under the same impact condition as that shown in Fig. 16 but with a 5 cm/s tangential velocity. The simulated solid surface temperature is shown in Fig. 18 with comparisons to the experimental measurements of Chen and Hsu (1995). It can be seen that with a small obliquity, there is a significant effect on the movement behavior of the droplet. Specifically, in this case, the droplet moves away from the impact center during the recoiling process, which leads to a faster recovery of the solid surface temperature.

The simulations are further conducted under the experimental conditions of Inada *et al.* (1985). In their experiments, 4.0 mm water droplets impact on a heated platinum surface at a temperature up to 420 °C. The subcooling degree

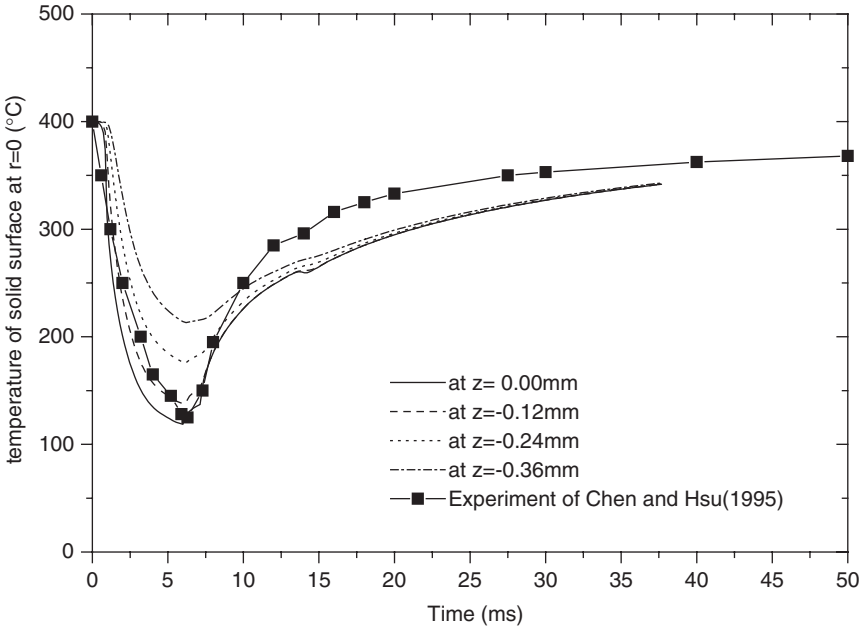

FIG. 18. Simulated solid surface temperatures compared with the experiments of Chen and Hsu (1995). The droplet impacts on the flat surface with a small tangential velocity (5 cm/s) as shown in Fig. 17.

of the droplet (δT_{sub}) can be varied from 2 °C to 88 °C. The droplet falls down 20 mm before it impacts on the surface, thus the velocity of the impact can be estimated as 64 cm/s, which gives a Weber number of about 25. In this simulation, the initial temperature of surface is fixed on 420 °C, which ensure the nonwetting contact between the droplet and the surface. Fig. 19 shows the simulated solid temperature compared with the measured value at two locations. T_1 and T_2 were measured at 0.28 and 0.74 mm depth beneath the surface (Inada *et al.*, 1985). Simulated surface temperatures agreed well with the measured T_1 and T_2; both decrease until 13–14 ms after the impact. The simulated temperature at the surface of the solid (T_w) is also shown in Fig. 19. The maximum temperature drop at the surface is about 60 °C, which occurs at about 13 ms after the impact.

C. Simulation of Droplet–Particle Collision in the Leidenfrost Regime

An efficient numerical model to describe the unsteady, 3-D fluid flow during the droplet–particle collision with evaporation is developed (Ge and Fan, 2005). From the numerical point of view, the droplet and solid surface need to be

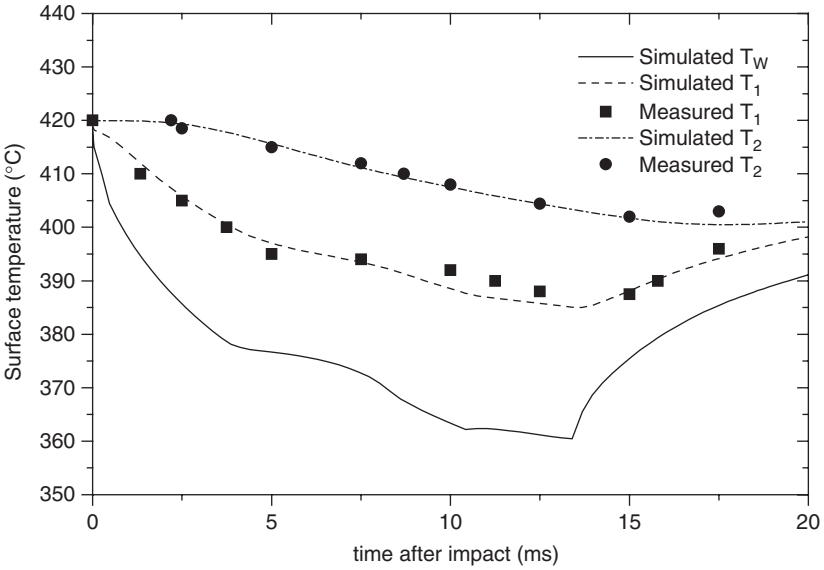

FIG. 19. Simulated solid surface temperatures compared with the experiments of Inada *et al.* (1985). T_1 and T_2 are the temperatures at locations inside the surface with $Z_1 = 0.28$ mm and $Z_2 = 0.74$ mm.

captured in the flow field and the solid-flow boundary condition at the particle surface needs to be satisfied. The numerical method adopted is a combination of the level-set approach and the IBM. The evaporation effect is accounted for by the vapor pressure force, which is calculated in a dynamics vapor-flow model. Energy balance equations in each phase are solved with interface boundary condition to give the temperature distribution and evaporation rate.

1. *Hydrodynamic Model with Level-Set Method*

In this model, two level-set functions (ϕ_d, ϕ_p) are defined to represent the droplet interface (ϕ_d) and the moving particle surface (ϕ_p), respectively. The free surface of the droplet is taken as the zero in the droplet level-set function $\phi_d(\vec{x}, t)$, and the advection equation (Eq. (3)) of the droplet level-set function (ϕd) is solved to capture the motion of the droplet surface. The particle level-set function (ϕp) is defined as the signed distance from any given point $\vec{x}$ in the Eulerian system to the particle surface:

$$\phi_\mathrm{p} = \left|\vec{x} - \vec{x}_0(t)\right| - R_\mathrm{p} \tag{78}$$

where $\vec{x}_0(t)$ is the position vector of the center of the particle and R_p the particle radius. With this definition, $\phi_p > 0$ when $\vec{x}$ is outside the particle, $\phi_p < 0$ when $\vec{x}$ is inside the particle.

The momentum equation for this 3-phase flow system in the Eulerian frame can be given by

$$\rho\left(\frac{\partial \vec{V}}{\partial t}+\nabla\cdot\vec{V}\vec{V}\right) = -\nabla p+\rho\vec{g}+\nabla\cdot(2\mu\tilde{D})+\sigma\kappa(\phi_{\mathrm{d}})\delta(\phi_{\mathrm{d}})\nabla\phi_{\mathrm{d}} + \vec{F}_{\mathrm{p}}(\phi_{\mathrm{p}})+\vec{F}_{\mathrm{vapor}} \tag{79}$$

In this equation, the presence of the solid particle in the fluid is represented by a virtual boundary body force field, $\vec{F}_{\mathrm{p}}(\phi_{\mathrm{p}})$, defined by the IBM which will be discussed in Section IV.C.2. $\vec{F}_{\mathrm{vapor}}$ is vapor pressure force exerting on the droplet–particle contact area due to the effect of the evaporation, which will be discussed in vapor-layer model of Section IV.C.3.

2. *Immersed-Boundary/Level-Set Method for Particle–Flow Interaction*

In the IBM, the presence of the solid boundary (fixed or moving) in the fluid can be represented by a virtual body force field $\vec{F}_{\mathrm{p}}(\phi_{\mathrm{p}})$ applied on the computational grid at the vicinity of solid–flow interface. Considering the stability and efficiency in a 3-D simulation, the direct forcing scheme is adopted in this model. Details of this scheme are introduced in Section II.B. In this study, a new velocity interpolation method is developed based on the particle level-set function (ϕ_{p}), which is shown in Fig. 20. At each time step of the simulation, the fluid–particle boundary condition (no-slip or free-slip) is imposed on the computational cells located in a small band across the particle surface. The thickness of this band can be chosen to be equal to 3Δ, where Δ is the mesh size (assuming a uniform mesh is used). If a grid point (like p and q in Fig. 20), where the velocity components of the control volume are defined, falls into this band, that is

$$\Delta x > \phi_{\mathrm{p}} > -\Delta x \tag{80}$$

the velocity at these points will be redefined using linear interpolation based on the velocity and particle level-set function (ϕ_{p}) at the neighboring grid point. At grid point p in Fig. 20, which is located in the band and outside the particle surface, the fluid velocity is determined by (for no-slip boundary condition):

$$U_{\mathrm{p}} = V_{\mathrm{p}}(t)+\frac{\phi_{\mathrm{p}}}{n}\sum_{i}^{n}\frac{U_{\mathrm{p}',i}-V_{\mathrm{p}}(t)}{\phi_{\mathrm{p}',i}} \tag{81}$$

where $U_{\mathrm{p}'}$ and $\phi_{\mathrm{p}'}$ are the fluid velocity and particle level-set function at grid point p′ (in Fig. 20). It should be noted that only the neighboring grid points located outside the band are chosen to interpolate the velocity at point p. The velocities at these points (p′) are obtained by solving the N-S equation like other points far from the interface. n is the total number of these neighboring points. It can be seen that when $\phi_{\mathrm{p}}=0$, meaning that the grid point p is right on the particle surface, the velocity at p is equal to the particle velocity: $U_{\mathrm{p}}=V_{\mathrm{p}}(t)$.

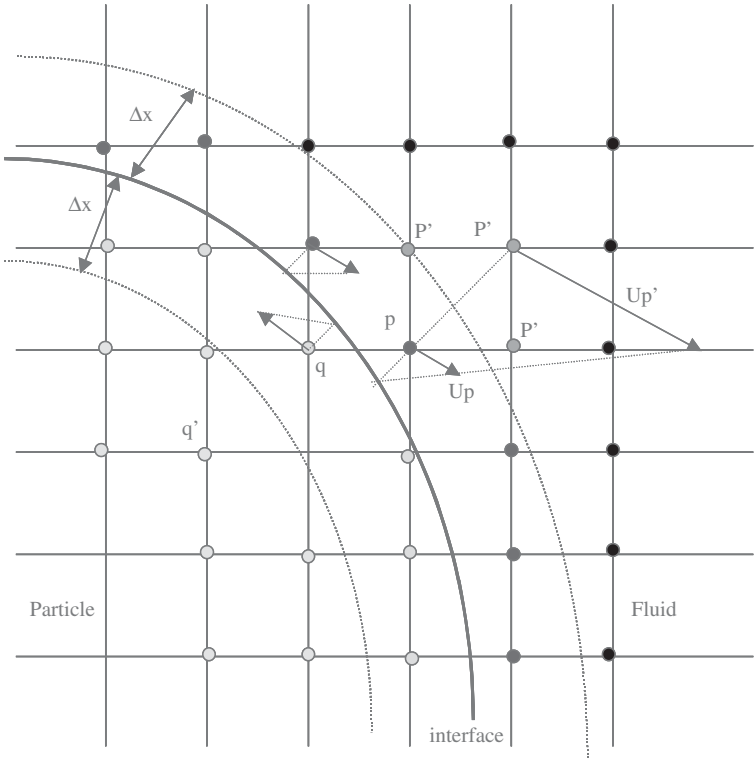

FIG. 20. Velocity interpolation scheme based on the particle level-set function.

The velocity at grid point q (in Fig. 20), which is located inside the small band and on the particle side, is determined by interpolating the fluid velocity at the neighboring grid points outside the particle surface:

$$U_{\mathrm{q}} = V_{\mathrm{p}}(t) + \frac{\phi_{\mathrm{q}}}{m} \sum_{i}^{m} \frac{U_{\mathrm{p},i} - V_{\mathrm{p}}(t)}{\phi_{\mathrm{p},i}} \tag{82}$$

where m is the total number of neighboring grid points which are located outside the particle surface.

3. *Vapor Layer and Heat-Transfer Model*

As the vapor flows in the direction along the spherical surface of the particle, a boundary layer coordinate (ξ, λ, ω) given in Fig. 21 is employed to describe the vapor-layer equation. In this coordinate, the continuity and momentum equations for incompressible vapor flows with gravitation terms neglected

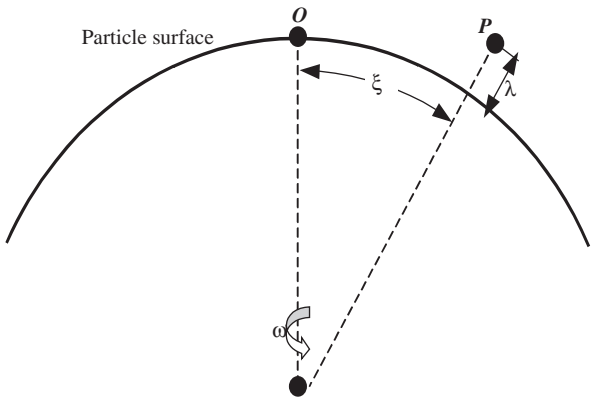

FIG. 21. Boundary layer coordinates.

are given by

$$\frac{\partial u_\xi}{\partial \xi} + \frac{\cot(\xi/R)}{R} u_\xi + \frac{2}{R} u_\lambda + \frac{\partial u_\lambda}{\partial \lambda} = 0 \tag{83}$$

$$u_\xi \frac{\partial u_\xi}{\partial \xi} + u_\lambda \frac{\partial u_\xi}{\partial \lambda} + \frac{u_\xi u_\lambda}{R} = -\frac{\partial}{\partial \xi}\left(\frac{P}{\rho}\right) - \nu\left(\frac{\partial^2 u_\lambda}{\partial \xi \partial \lambda} - \frac{2}{R}\frac{\partial u_\xi}{\partial \lambda} - \frac{\partial^2 u_\xi}{\partial \lambda^2}\right) \tag{84}$$

$$\begin{aligned} u_\xi \frac{\partial u_\lambda}{\partial \xi} + u_\lambda \frac{\partial u_\lambda}{\partial \lambda} - \frac{u_\xi^2}{R} = & -\frac{\partial}{\partial \lambda}\left(\frac{P}{\rho}\right) + \frac{\nu}{R}\left[R\frac{\partial^2 u_\lambda}{\partial \xi^2} - \frac{\partial u_\xi}{\partial \xi} - R\frac{\partial^2 u_\xi}{\partial \xi \partial \lambda}\right. \\ & \left. + \cot\left(\frac{\xi}{R}\right)\left(\frac{\partial u_\lambda}{\partial \xi} - \frac{u_\xi}{R} - \frac{\partial u_\xi}{\partial \lambda}\right)\right] \end{aligned} \tag{85}$$

where u_ξ, u_λ are the vapor-flow velocities in ξ and λ direction, respectively.

Based on the assumptions and the order of magnitude analysis described in Section IV.A.2, and following the similar procedure of solution, the averaged vapor-flow velocity is given by

$$\bar{u}_\xi(\xi) = \Omega \int_0^1 \Phi_\delta \mathrm{d}\eta = \frac{1}{2} u_{l\delta}(\xi) - \frac{\delta^2}{12\gamma}\left(1 - \frac{3}{20} Re_\delta\right)\frac{\partial}{\partial \xi}\left(\frac{p}{\rho}\right) \tag{86}$$

The vapor continuity equation can be expressed by

$$\bar{u}_\xi(\xi) = \frac{1}{\xi \delta(\xi)} \int_0^\xi \xi' u_{\lambda\delta}(\xi')\, \mathrm{d}\xi' \tag{87}$$

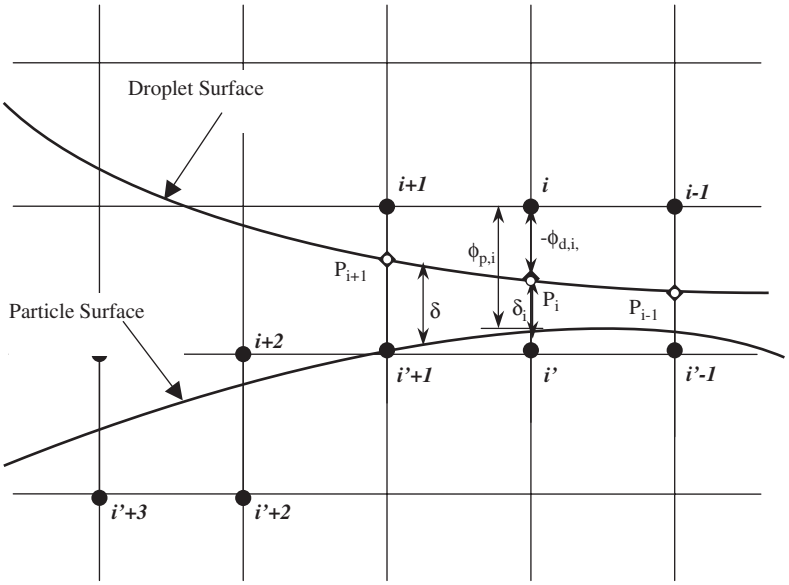

FIG. 22. Scheme for determining the thickness of the vapor layer.

The $u_{\lambda\delta}(\xi)$ is calculated using Eq. (55). The pressure distribution in the vapor layer can be obtained by solving Eqs. (86) and (87). In this procedure, the thickness of the vapor layer ($\delta(\xi)$) and the extent of the layer (ξ_b) are obtained through a vapor-layer identification scheme based on the particle and droplet level-set function. Fig. 22 illustrates the details of the scheme.

As the particle is in motion, at every time step, a series of grid points near the particle surface are first identified to measure the vapor layer. As shown in Fig. 22, these grids points are in a small band around the surface and can be outside the surface ($\ldots,i-1,\ i,\ i+1,\ i+2,\ldots$) or inside the surface ($\ldots,\ i'-1,\ i',\ i'+1,\ i'+2,\ldots$). If the droplet surface is represented by points ($\ldots,\ P_{i-1},\ P_i,\ P_{i+1},\ldots$) in Fig. 22 and point P_i is located on the mesh line between the mesh knots i and i', the vapor-layer thickness at P_i can be calculated based on the values of the level-set function at i and i' defined as ($\phi_{d,i},\phi_{p,i}$) and ($\phi_{d,i'},\phi_{p,i'}$), respectively. Since the level-set function is the signed distance from the computation knots to the droplet and particle surface after the redistance process is performed, the vapor-layer thickness (δ_i) at P_i can be estimated by

$$\delta_i = \frac{\phi_{d,i} + \phi_{p,i} + \phi_{d,i'} + \phi_{p,i'}}{2} \tag{88}$$

The heat-transfer model described in Sections IV.A.3 and IV.B.2 can be applied to calculate the temperature distribution inside the droplet and energy

balance at the interface. Inside the particle, the heat-conduction equation is

$$\frac{\partial T}{\partial t} = \alpha_s \nabla \cdot \nabla T \tag{89}$$

where α_s is the thermal diffusivity of particle. When the particle surface is in contact with the droplet through the vapor layer, the boundary condition at the particle surface is given by

$$k_v \frac{T_{ss} - T_{ds}}{\delta} = -k_s \vec{n}_p \cdot \nabla_p T_s \tag{90}$$

where $\vec{n}_p$ is the normal vector of the particle surface, $\nabla_p T$ the temperature gradient which is evaluated only on the particle side. This boundary condition, Eq. (90) is imposed on the computational cells, which are located in a small band near the particle surface on the solid side.

4. Results and Discussion

Droplet–particle collision conditions under which experiments are conducted are simulated in this study. In the experiment, the brass particle is heated on a heating plate with adjustable temperature settings, and a high-speed camera capable of capturing 500 frames per second will be used to record the droplet–particle collision process. A droplet is formed by the use of the syringe with various needle sizes. In the experiments, acetone droplets with 1.6–2.2 mm diameter impact onto the brass particles of sizes 5.5 mm or 3.6 mm.The particle temperature is 200 °C–300 °C, which is much higher than the boiling point of acetone and ensures that the contact is nonwetting.

The simulation is conducted on uniform Cartesian meshes ($\Delta x = \Delta y = \Delta z = \Delta$). The mesh sizes in this study are chosen to give a resolution of CPR = 15. Fig. 23 shows the comparison of the photographs with simulated images for a 2.1 mm acetone droplet impact onto a 5.5 mm brass particle of 250 °C. The impact velocity is 45 cm/s. The initial temperature of the droplet is close to the boiling point of acetone (56 °C). A comparison of the images shows that the impact process is predicted well by this model. Similar to the impact on a flat surface, the droplet spreads on the particle surface at the first stage (0–5.5 ms), then recoils due to the vapor pressure force and surface tension force (7.5–13.5 ms), and eventually rebounds away from the particle (17.5–27.5 ms). The droplet film reaches the maximum extent at about 7.0 ms, by which time the radius of droplet–particle contact area is about 1.5 times that of the original radius of the droplet. The total contact time is about 17 ms, which is relevant to the first-order vibration period of the oscillating drop.

Fig. 24 shows the collision process between a moving particle (1.5 mm in diameter) and a large water droplet. A water droplet 2.5 mm in diameter has an initial velocity of 25 cm/s and an initial temperature of 100 °C. The initial velocity and temperature of the particle are 25 cm/s and 400 °C, respectively.

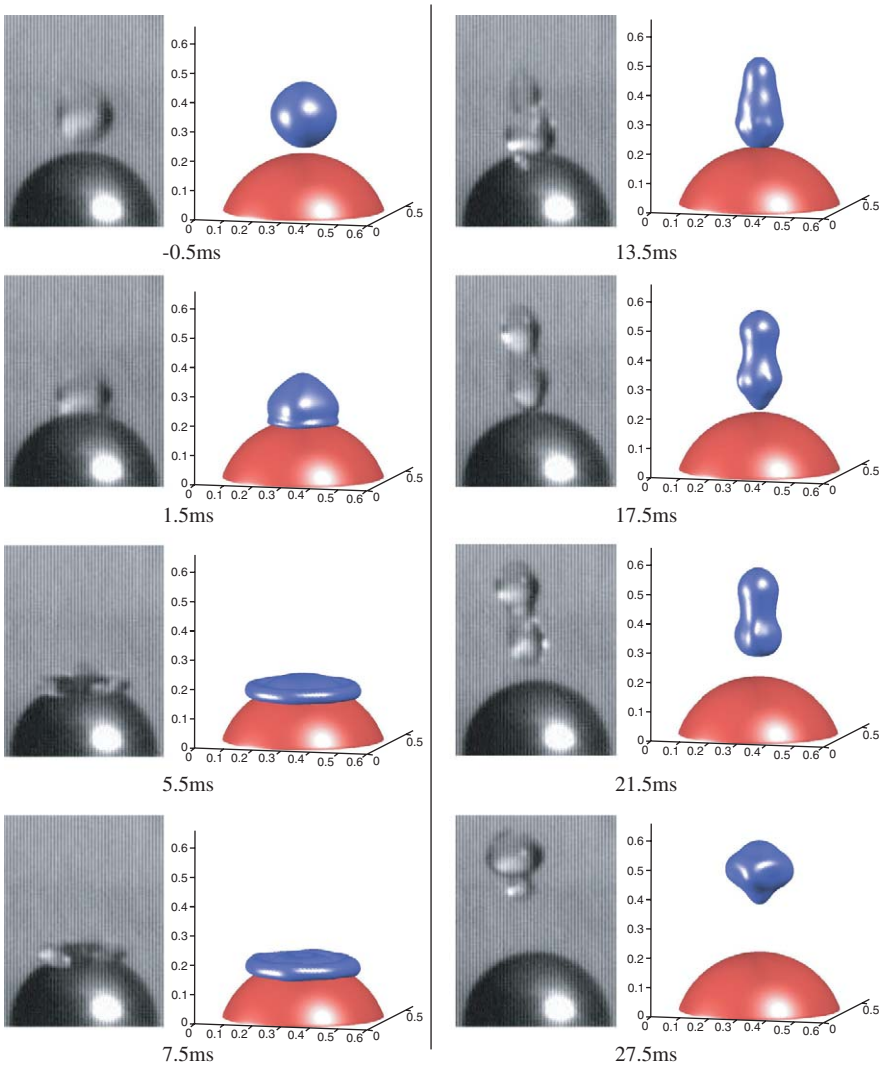

FIG. 23. Experimental photos (left) and simulated images (right) of the 2.1 mm acetone droplet impact on 5.5-mm particle at 250 °C. Impact velocity $V = 45\,\text{cm/s}$.

The physical properties of the particle are the same as FCC particles. The simulation is conducted using a $140 \times 140 \times 200$ rectangular mesh covering a $7\,\text{mm} \times 7\,\text{mm} \times 10\,\text{mm}$ computational domain. Both the 3-D images and the temperature field are shown in this figure.

It can be seen in this figure that since the inertia (mass) of the particle is smaller than that of the droplet, the particle velocity decreases rapidly as soon as the particle collides with the droplet. After the collision, the surface tension of

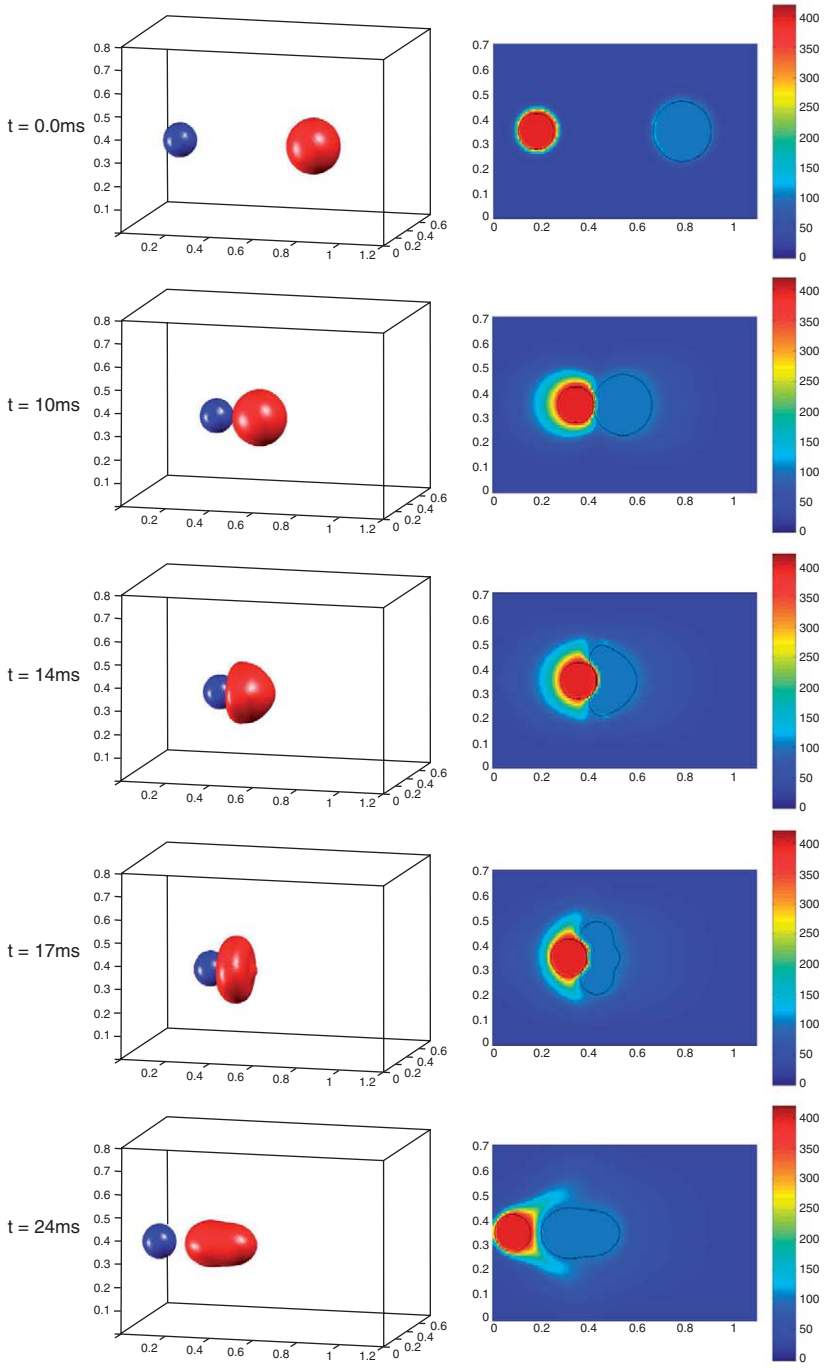

FIG. 24. Particle and droplet collision at the same initial velocity. The images on the right show the temperature field.

the droplet and the vapor-layer pressure induced by the evaporation drive the particle to the inverse direction. Since the Weber number of the collision is not very large ($We = 15$), the droplet only undergoes small deformation without splashing. After collision, the droplet still moves along its original path with a decreased velocity, while the rebounding velocity of the particle is larger than that of the droplet. It can also be found that the temperature drop of the particle is not significant in this condition.

V. Concluding Remarks

The most significant advantage of the level-set method and the IBM in solving 3-D, three-phase flow problems is that the governing equations can conveniently be discretized and solved on fixed, regular structured grids, rather than resorting to the classic body-fitted mesh approach. These methods are efficient in utilizing computational resources while retaining the accuracy of the computational results. The level-set method implicitly captures the motion of the interface by solving the advection equation of the level-set function, and can be easily implemented for 3-D interface tracking. The level-set methods are particularly effective in handling flow problems that involve changes in the topology of evolving interfaces, and in which the speed of the interface is sensitive to local surface geometry, such as curvature and normal vector. Although, like other front-capture techniques, the level-set method may suffer from some problems associated with the preservation of mass conservation (Puckett *et al.*, 1997), the method is able to accurately compute interfacial flows with surface tension force and other complex physical forces acting on the front. In the conventional IBM, the moving front is represented by a finite number of discrete Lagrangian markers along the interface, which move in the flow. In general, this arrangement has the property of preservation of the clear interface position and hence mass conservation; however, with this arrangement, it is difficult to trace the interface with complicated shape and topological change in three dimensions. The combination of the level-set method and the IBM as described in this study can allow accuracy in interface movement, as well as conservation in moving object mass when simulating the complex three-phase interaction systems.

In system 1, the 3-D dynamic bubbling phenomena in a gas–liquid bubble column and a gas–liquid–solid fluidized bed are simulated using the level-set method coupled with an SGS model for liquid turbulence. The computational scheme in this study captures the complex topological changes related to the bubble deformation, coalescence, and breakup in bubbling flows. In system 2, the hydrodynamics and heat-transfer phenomena of liquid droplets impacting upon a hot flat surface and particle are analyzed based on 3-D level-set method and IBM with consideration of the film-boiling behavior. The heat transfers in

each phase are solved using a microscale vapor-flow model which is applied to determine the vapor pressure force during the contact process between the droplet and the superheated surface. The simulation model developed in this study is capable of reproducing the droplet impaction process with significant heat transfer and phase change (evaporation). Both the saturated impact and the subcooling impact are considered. The simulation results are found to be in good agreement with the experimental measurements of the droplet deformation process and the surface-temperature variation.

Nomenclature

NOTATION

C_D	modified drag coefficient
C_{D0}	drag coefficient
C_s	Smagorinsky coefficient
$\tilde{D}$	stress tensor
d	distance function (or diameter)
d_p	diameter of particle
f_{am}	added mass force
f_d	fluid–particle interaction force
f_{dr}	drag force
f_σ	surface tension force
g	gravitational acceleration
H_β	heaviside function
k	heat conductivity
Kn	Knudsen number
l	length scale
L_c	latent heat
m_p	mass of particle
$\dot{m}$	mass evaporation rate
n	normal vector
p	pressure
Pr	Prandtl number
q	heat flux (or virtual mass source)
R	radius of the droplet
Re	particle Reynolds number
S	shear strain rate
T	temperature
t	time
U	velocity scale of the vapor flow
u	velocity of the vapor flow

$\boldsymbol{V}$	velocity (or volume)
We	Weber number
x	position vector

GREEK LETTERS

α	thermal diffusivity
Δ	grid size
Γ	gas–liquid interface
Φ	function defined in vapor-layer model (4.7)
Ω	cell volume (or function defined in vapor-layer model (4.7))
β	half of the thickness of the interface
δ	δ function (or the thickness of the vapor-layer or thermal boundary layer)
ε	void fraction
ϕ	level-set function
κ	curvature of the surface
λ	constant defined in Eq. (24) (or coordinate defined in vapor-layer model)
μ	molecular viscosity
ν_{T}	kinematic turbulent viscosity
ρ	density
σ	surface tension (or thermal accommodation coefficient)
τ	viscous stress tensor, artificial time
ξ	coordinate defined in vapor-layer model
η	dimensionless variable defined in Eq. (46)
ν	kinematic viscosity of vapor flow

SUBSCRIPTS AND SUPERSCRIPTS

b	boundary
d	droplet
g	gas phase
l	liquid phase
o	initial
p	particle
r	radial direction
s	solid
v	vapor phase

ξ	vapor-layer coordinate
λ	vapor-layer coordinate
Γ	gas–droplet interface
ij	cell index
k	particle index
sa	saturated
sg	sub-grid scale

REFERENCES

Agresar, G., Linderman, J. J., Triggvason, G., and Powell, K. G. *J. Comp. Phys.* **143**, 346 (1998).
Amsden, A. A., and Harlow, F. H. *J. Comp. Phys.* **3**, 80 (1968).
Anderson, T. B., and Jackson, R. *Ind. Eng. Chem. Fundam.* **6**, 525–539 (1967).
Biance, A. -L., Clanet, C., and Quere, D. *Phys. Fluids* **15**(6), 1632–1637 (2003).
Bird, G. A., "Molecular Gas Dynamics". Clarendon Press, Oxford, UK (1976).
Brackbill, J. U., Kothe, D. B., and Zemach, C. *J. Comp. Phys.* **100**, 335 (1992).
Bussmann, M., Mostaghimi, J., and Chandra, S. *Phys. Fluids* **11**(6), 1406–1417 (1999).
Bussmann, M., Mostaghimi, J., and Chandra, S. *Phys. Fluids* **12**(12), 3121–3132 (2000).
Chandra, S., and Avedisian, C. T. *Proc. R. Soc. Lond. A* **432**, 13–41 (1991).
Chen, C., and Fan, L. -S. *AIChE J* **50**, 288–301 (2004).
Chen, J. C., and Hsu, K. K. *J. Heat Transfer* **117**, 693–697 (1995).
Chen, Y. -M., and Fan, L. -S. *Chem. Eng. Sci.* **44**, 2762 (1989a).
Chen, Y. -M., and Fan, L. -S. *Chem. Eng. Sci.* **44**, 117 (1989b).
Crowe, C. T., Sharma, M. P., and Stock, D. E. *J. Fluids Eng.* **99**, 325 (1977).
Crowe, C., Sommerfeld, M., and Tsuji, Y., "Multiphase Flows with Droplets and Particles". CRC Press, NY (1998).
Dandy, D. S., and Leal, L. G. *J. Fluid Mech.* **208**, 161 (1989).
Delnoij, E., Kuipers, J. A. M., and Van Swaaij, W. P. M. *Chem. Eng. Sci.* **52**, 3623 (1997).
Fadlun, E. A., Verzicco, R., Orlandi, P., and Yusof, J. M. *Comp. Phys.* **161**, 35–60 (2000).
Fan, L. S., "Gas–Liquid–Solids Fluidization Engineering". Butterworths, Stoneham, MA (1989).
Fan, L. -S., and Tsuchiya, K., "Bubble Wake Dynamics in Liquid and Liquid–Solid Suspensions". Butterworth-Heinemann, Stoneham, MA (1990).
Fan, L. -S., Lau, R., Zhu, C., Vuong, K., Warsito, W., Wang, X., and Liu, G. *Chem. Eng. Sci.* **56**, 5871–5891 (2001).
Feng, J., Hu, H. H., and Joseph, D. D. *J. Fluid Mech.* **261**, 95–134 (1994a).
Feng, J., Hu, H. H., and Joseph, D. D. *J. Fluid Mech.* **277**, 271–301 (1994b).
Feng, Z. -G., and Michaelides, E. E. *J. Comput. Phys.* **202**, 20–51 (2005).
Fujimoto, H., and Hatta, N. *J. Fluids Eng.* **118**, 142–149 (1996).
Fukai, J., Shiiba, Y., Yamamoto, T., and Miyatake, O. *Phys. Fluids* **7**(2), 236 (1995).
Ge, Y., and Fan, L. -S. *Phys. Fluids* **17**, 027104 (2005).
Goldstein, D., Handler, R., and Sirovich, L. *J. Comp. Phys.* **105**, 354 (1993).
Gottfried, B. S., Lee, C. J., and Bell, K. *J. Int. J. Heat Mass Transfer* **9**, 1167–1187 (1966).
Groendes, V., and Mesler, R. Proceedings of the 7th International Heat Transfer Conference, Munich, Federal Republic of Germany 1982, 1982, pp. 131–136.
Harlow, F. H., and Welch, J. E. *Phys. Fluid* **8**, 2182 (1965).
Harlow, F. H., and Shannon, J. P. *J. Appl. Phys.* **38**, 3855 (1967).
Harvie, D. J. E., and Fletcher, D. F. *Int. J. Heat Mass Transfer* **44**, 2633–2642 (2001a).
Harvie, D. J. E., and Fletcher, D. F. *Int. J. Heat Mass Transfer* **44**, 2643–2659 (2001b).

Harvie, D. J. E., and Fletcher, D. F. *J. Heat Transfer* **123**, 486–491 (2001c).
Hatta, N., Fujimoto, H., Kinoshita, K., and Takuda, H. *J. Fluids Eng.* **119**, 692–699 (1997).
Hirt, C. W., Amsden, A. A., and Cook, J. L. *J. Comput. Phys.* **14**, 227 (1974).
Hirt, C. W., and Nichols, B. D. *J. Comput. Phys.* **39**, 201 (1981).
Hoomans, B. P. B., Kuipers, J. A. M., Briels, W. J., and van Swaaij, W. P. M. *Chem. Eng. Sci.* **51**, 99–118 (1996).
Inada, S., Miyasaka, Y., and Nishida, K. *Bull. JSME* **28**, 2675–2681 (1985).
Inada, S., Miyasaka, Y., Sakamoto, K., and Hojo, K. *J. Chem. Eng. Japan* **21**, 463 (1988).
Jackson, R., "The Dynamics of Fluidized Particles". Cambridge University Press, NY (2000).
Jamet, D., Lebaigue, O., Coutris, N., and Delhaye, J. *M. J. Comput. Phys.* **169**, 624 (2001).
Joseph, D. D., and Lundgren, T. S. *Int. J. Multiphase flow* **16**, 35–42 (1990).
Kanai, A., and Mtyata, H. "Numerical simulation of bubbles in a boundary layer by Maker-Density-Function". Proceedings of the 3rd International Conference on Multiphase Flow, Lion, France (1998).
Karl, A., Anders, K., Rieber, M., and Frohn, A. *Part. Part. Syst. Charact.* **13**, 186–191 (1996).
Kashiwa, B. A., Padial, N. T., Rauenzahn, R. M., and Vanderheyden, W. B. Los Alamos National Laboratory Research Report, LA-UR-93-3922 (1994).
Kim, J., Kim, D., and Choi, H. *J. Comput. Phys.* **171**, 132–150 (2001).
Kothe, D. B., and Rider, W. J. Los Alamos National Laboratory Research Report, LA-UR-94-3384 (1995).
Kunii, D., and Levenspiel, O., "Fluidization Engineering". 2nd ed Butterworth-Heinemann, Boston (1991).
Lai, M. -C., and Peskin, C. S. *J. Comput. Phys.* **160**, 705–719 (2000).
Lapin, A., and Lübbert, A. *Chem. Eng. Sci.* **49**, 3661 (1994).
Li, Y., Zhang, J., and Fan, L. -S. *Chem. Eng. Sci.* **54**, 5101 (1999).
McHyman, J. *Physica D* **12**, 396 (1984).
Mehdi-Nejad, V., Mostaghimi, J., and Chandra, S. *Phys. Fluids* **15**(1), 173–183 (2003).
Mittal, R., and Iaccarino, G. *Annu. Rev. Fluid Meth.* **37**, 239–261 (2005).
Monaghan, J. *J. Comput. Phys.* **110**, 399 (1994).
Mudde, R. F., and Simonin, O. *Chem. Eng. Sci.* **54**, 5061 (1999).
Osher, S., and Sethian, J. A. *J. Comput. Phys.* **79**, 12 (1988).
Pasandideh-Ford, M., Bhola, R., Chandra, S., and Mostaghimi, J. *Int. J. Heat Mass Transfer* **41**, 2929–2945 (1998).
Pasandideh-Ford, M., Aziz, S. D., Chandra, S., and Mostaghimi, J. *Int. J. Heat Fluid Flow* **22**, 201 (2001).
Peskin, C. S. *J. Computat. Phys.* **25**, 220 (1977).
Puckett, E. G., Almgren, A. S., Bell, J. B., Marcus, D. L., and Rider, W. J. *J. Computat. Phys.* **100**, 269 (1997).
Qiao, Y. M., and Chandra, S. *Int. J. Heat Mass Transfer* **39**(7), 1379–1393 (1996).
Rowe, P. N., and Henwood, G. A. *Part. 1 Trans. Inst. Chem. Eng* **39**, 43 (1961).
Sato, T., and Richardson, S. M. *Int. J. Numer. Meth. Fluids* **19**, 555 (1994).
Scardovelli, R., and Zeleski, S. *Ann. Rev. Fluid Mechanics* **31**, 567 (1999).
Sethian, J. A., and Smereka, P. *Annu. Rev. Fluid Meth.* **35**, 341–372 (2003).
Smagorinsky, J. *Mon. Weather Rev.* **91**, 99 (1963).
Sokolichin, A., and Eigenberger, G. *Chem. Eng. Sci.* **49**, 5735 (1994).
Sokolichin, A., and Eigenberger, G. *Chem. Eng. Sci.* **54**, 2273 (1999).
Sussman, M., Smereka, P., and Osher, S. *J. Comput. Phys.* **114**, 146 (1994).
Sussman, M., Fatemi, E., Smereka, P., and Osher, S. *Computers Fluids* **114**, 146 (1998).
Sussman, M., and Fatemi, E. *SIAM J. Sci. Comput.* **20**, 1165 (1999).
Tryggvason, T., Bunner, B., Esmaeeli, A., Juric, D., Al-Rawahi, N., Tauber, W., Han, J., Nas, S., and Jan, Y. -J. *J. Comput. Phys.* **169**, 708–759 (2001).
Tsuji, Y., Kawaguchi, T., and Tanaka, T. *Powder Technol* **77**, 79–81 (1993).

Udaykumar, H. S., Kan, H. -C., Shyy, W., and Tran-Son-Try, R. *J. Comput. Phys.* **137**, 366–405 (1997).
Unverdi, S. O., and Tryggvason, G. J. *Computat. Phys.* **100**, 25 (1992a).
Unverdi, S. O., and Tryggvason, G. *Physica D* **60**, 70 (1992b).
Wachters, L. H. J., and Westerling, N. A. J. *Chem. Eng. Sci.* **21**, 1047–1056 (1966).
Wen, C. Y., and Yu, Y. H. *Chem. Eng. Prog.* **62**, 100 (1966).
Yabe, T. "Interface Capturing and Universal Solution of Solid, Liquid and Gas by CIP Method". Proceedings of the High-Performance Computing of Multi-Phase Flow, Tokyo, July 18–19, 1997.
Ye, T., Mittal, R., Udaykumar, H. S., and Shyy, W. *J. Computat. Phys.* **156**, 209–240 (1999).
Yusof, J. M. Combined immersed boundaries/B-splines methods for simulations of flows in complex geometries. *CTR Annual Research Briefs, NASA Ames/Stanford University* (1997).
Zenit, R., and Hunt, M. *J. Fluids Eng.* **121**, 179 (1999).
Zhang, D. Z., and Prosperetti, A. *J. Fluid Mech.* **267**, 185–219 (1994).
Zhang, J., Fan, L. -S., Zhu, C., Pfeffer, R., and Qi, D. *Powder Technol* **106**, 98 (1999).
Zhang, Z., and Prosperetti, A. *J. Appl. Mech.-Trans. ASME* **70**, 64–74 (2003).
Zhu, C., Wang, X., and Fan, L. -S. *Powder Technol* **111**, 79–82 (2000).